Moisture transportation for extreme precipitation

On how dynamics enhances precipitation intensification in a warmer climate in the Netherlands

MSc. thesis green light meeting report

Falco P. Bentvelsen

TUDelft

Moisture transportation for extreme precipitation

On how dynamics enhances precipitation intensification
in a warmer climate in the Netherlands

by

Falco P. Bentvelsen

student number: 4158040

to obtain the degree of Master of Science

at Delft University of Technology

to be defended publicly on October 22, 2021 at 16:00

Committee chair:	Pier Siebesma	TU Delft, KNMI, chair
Daily supervisor:	Geert Lenderink	TU Delft, KNMI
Committee members:	Marc Schleiss	TU Delft
	Ruud van der Ent	TU Delft
Institution:	Delft University of Technology	
	Faculty of Civil Engineering	
	Department of Geoscience & Remote Sensing	

An electronic version of this thesis is available at https://repository.tudelft.nl/
Clouds over Delft city hall on June 18th 2021, credits to CAPE1450J/kg

TUDelft

Acknowledgements

Abstract

It is well understood that precipitation extremes will increase in a warming climate. On (sub-)hourly timescales, the apparent scaling of precipitation extremes is stronger than expected from the Clausius-Clapeyron relation. Here, we focus on a common hypothesis which states that feedbacks from the local dynamics of clouds are responsible.

The effects of climate change on intensification of extreme precipitation in the Netherlands are modeled using the Dutch Atmospheric Large Eddy Simulation (Lochbihler et al. 2019). The objective is to understand more about extreme precipitation events in a warming climate in the Netherlands. A feedback loop is proposed in which cold-pools increase precipitation intensification with super-CC scaling.

Atmospheric conditions from a composite of days with extreme precipitation are perturbed. The entire atmospheric temperature column is warmed and cooled by 4 degrees Kelvin under constant relative humidity. The convective precipitation is described with a 10 minute timescale. A period of organized convection in the simulations is selected for comparison between the simulations. In this timeframe of extreme precipitation, the yield increases 8.5% per degree Kelvin.

Convection grows deeper and updrafts in the clouds become stronger with warming. The updrafts that are the most representative of precipitation yield increase in velocity by 4.7% per degree Kelvin. At 7 km height, updraft speeds increase up to 20.7 % per degree Kelvin.

Moisture transport occurs predominantly low in the clouds, near cloud base. With warming, more moisture is transported higher up in the clouds. Moisture transport near the surface increases along organized gustfront lines. On average the increase in transport by updrafts in the sub-cloud layer is dominated by increased moisture rather than due to strong updrafts becoming stronger. The moisture that is concentrated into convective cores coincides with intenser precipitation cores. With warming the subsiding motions accelerate and a stronger drying effect is present around precipitation cores. Cold-pools become stronger, forming bigger gustfront structures.

Contents

Glossary

apparent scaling The relative increase of precipitation per degree of warming as determined from observations. Precipitation is paired with surface temperature or dew point temperature observations, and dependencies of extremes on (dew point) temperature are derived. Lenderink et al., 2021 1, 6–8, 17, 48

autoconversion The change of moisture from cloud condensed water to precipitation. 10

climate scaling Long-term changes to precipitation extremes due to climate change. In Lenderink et al. (2021), a differentiation is made between climate scaling and apparent scaling. Climate scaling is calculated with models. For this work the term is also adopted for the modelled increase of vertical velocities. Climate scaling coefficients α expres the modelled relative increase per Kelvin of warming. 4, 8, 11, 12, 14, 28–36, 38, 47–49, 52, 53, 58

Cloud Resolving Model Model type that has fine enough resolution to resolve (large) individual clouds. ix, 4, 17

coefficient of determination The proportion of the variation in the a variable that is predictable from another variable. It gives a quality estimate for a linear relationship between two variables. Can range between 0 and 1, in which 0 means no correlation and 1 means perfect linear correlation. The variables are then fully dependent on each other and can be considered to be one and the same. 31–33, 39, 40, 43, 44, 58

cold-pool An expanding volume of air near the surface initiated by a downdraft of relatively cold and dry air that is spreading outward when reaching the surface. 2–6, 12–15, 30, 31, 37–39, 42, 45, 51, 52

condensation rate Rate at which water vapor transforms into cloud condensed water. 11

convection Mass motions in a fluid such as the atmosphere, driven by buoyancy or mechanical forcing resulting in transport and mixing of the properties of that fluid. 14, 31, 36, 43, 50–52

convergence When an excess of mass of air (or moisture) flows into a volume of atmosphere, this is called convergence (or moist convergence). It is the integral of the transport flux through the boundary, into that volume. 3, 9–11, 14, 15, 19, 20, 23, 24, 37, 38, 40

deep cloud Clouds of great vertical extent, cumulonimbus clouds asociated with thunderstorms are a prime example. 14

dew point temperature Temperature a volume of air would have if it was cooled at constant pressure until saturation is reached. 6–8, 15, 17, 18

dry static energy Thermodynamic variable that an unsaturated parcel of dry air would have if brought adiabatically and from its initial state to a reference height. Similar to potential temperature, except that the concept of static energy assumes that any kinetic energy is locally dissipated into heat. 10, 62

equivalent potential temperature Temperature that is conserved during changes of an air parcel's pressure, even if water vapor condenses during that pressure change. 22

gust front A semi-linear region near the surface with strong horizontal and vertical wind speeds. 2, 3, 13, 15, 37–39, 41, 44, 51–53

lagrangian A lagrangian perspective for an air parcel follows it along the path it takes. Also known as the total derivative. It is the first order derivative with respect to time and the three spatial dimensions x,y,z 54, 62

Large Eddy Simulation Model type that is capable of resolving clouds and the turbulent eddies that contain most of the kinetic energy, typically 90%. The smaller eddies are parameterized for computational efficiency. An eddy is the swirling of a fluid and a reverse current, a vortex. ix, 2, 4, 6, 10, 14, 17, 53

mesoscale Size range between tens and a hundreds of kilometers, examples of mesoscale weather systems are thunderstorms, squal lines and cold-pools. 14

mixing ratio The ratio of the mass of a variable atmospheric constituent, e.g. water vapor, to the mass of dry air. Closely resembles specific humidity and can be assumed to be the same. 62, 63

organized phase The timeperiod of the simulation in which precipitation is organized into big cell structures. Described in Lochbihler et al. (2019) 30–32, 35, 36, 41, 45–49, 58, 60

precipitable water The depth of water in a column of the atmosphere, if all the water in that column precipitated out. 23

precipitation Water falling from the sky, whether it be in liquid form (rain) or solid form (snow, hail, etcetera). 2, 3, 8–10, 14, 15, 21–23, 34, 50, 51, 62, 63

precipitation efficiency The fraction of precipitation falling on the surface of the earth per amount of moisture transported into the clouds. 9, 62, 63

Probable Maximum Precipitation The expected greatest depth of precipitation that might fall. It is for a given duration that is physically possible over a given size storm area at a particular geographical location at a certain time of year. 8

relative humidity The percentage of water vapor specific humidity per saturation specific humidity. At ~100% relative humidity, clouds are formed. 3, 7, 9, 18

saturation specific humidity The concentration of moisture in a mass of air at which the air will not hold any more water vapor and consequently, the excess moisture will be converted into liquid water or ice. 6, 9, 22, 62

scaling The overarching concept of the relative increase of a quantity with (dew point) temperature. Contains climate schaling, which is determined from model results and apparent scaling, which is derived from observations. The relative increase of a quantity is usually precipitation intensity. 1, 2, 8–10, 12, 14, 17, 53

specific humidity The mass of water in a mass of air including the mass of water. 2, 20, 22, 25, 46–48, 63

synoptic scale Size range between hundreds and a few thousand kilometers, Low- or High pressure systems in a mid-latitude weather forecast, the region of influence of such a weather system is on the synoptic scale. 8, 17, 19

updraft Small scale current of air with wind that is blowing skyward. 3, 5, 9, 15, 17, 23, 30, 31, 34, 36, 41, 44, 50, 53

wind shear For this work only horizontal wind shear is considered. Horizontal wind shear is a difference in horizontal wind speed or direction over a short vertical distance in the atmosphere. 20, 37, 51, 52, 54

Acronyms

AMS American Meteorological Society 2

CC Clausius Clapeyron 6–12, 14, 32, 48

COLD Climate scenario with 4 Kelvin cooling compared to REF of the initial vertical atmospheric profile 18, 19, 30, 31, 34, 36, 37, 40–45, 47, 50, 51

CRM Cloud Resolving Model 4, 17

DALES Dutch Atmospheric Large Eddy Simulation 5, 18, 22, 23, 27, 50

LES Large Eddy Simulation 2, 4, 6, 17, 53

NWP Numerical Weather Prediction 10, 17, 53

PMP Probable Maximum Precipitation 8

RCE Radiative-Convective Equilibrium 4, 17

REF Reference climate scenario constructed from a composite of extreme precipitating days 18, 19, 30, 31, 34, 36, 41, 42, 47, 50, 60

RH Relative Humidity 5–7

WARM Climate scenario with 4 Kelvin warming compared to REF of the initial vertical atmospheric profile 18, 19, 30–32, 34, 37, 38, 41, 42, 44–47, 50, 51, 58

1

General introduction

Atmospheric science uses modeling and observations to do justified predictions on the future state of the weather and climate. Accurate knowledge on extreme precipitation rates is required for the design of drainage systems. In a warming climate, precipitation extremes will increase in the Netherlands. The exact amount of increase per degree of warming is still uncertain for sub-hourly timescales. This work aims to improve understanding of how extreme precipitation in the Netherlands will intensify by considering convective dynamics.

This chapter gives a short introduction to the why, what and how of this research. The motivation 'why' is given in Section 1.1. Section 1.2 gives the research aim. Some high level foundational knowledge is then given in Section 1.3. After which it is made explicit 'what' the research questions are in Section 1.4. The 'what' is further made explicit with hypotheses to these research questions in Section 1.5. Following that, the 'how' is introduced with an approach and outline in Section 1.7.

A general introduction is short and easily readable. Therefore, the underlying literature is not treated extensively here, but presented in Chapter 2 with a deepening of the concepts introduced in this chapter. Besides that, concepts new to the reader may also be found in the glossary in the frontmatter of this report.

1.1. Motivation

Water drops and ice crystals seemingly defy gravity in the sky. Every day there is a chance of letting one's imagination free on what's happening in the clouds. Sometimes these majestic friends in the firmament can be unruly though, and release torrential downpours. Extreme precipitation events can lead to flooding. Drainage systems should be designed such that they can handle the inputs from storms in a future climate. Therefore, knowledge of the rainfall intensity is essential for the design of urban drainage systems.

It is well understood that precipitation extremes will increase in a warming climate (e.g. O'Gorman, 2015). This is primarily based on the Clausius-Clapeyron (CC) relation which states that warmer air can contain more water vapor at a rate of 6-7 % per degree Celsius of temperature (CC scaling). In fact, at larger spatial and longer temporal scales, changes in precipitation are often found to be close to the CC scaling, both in model projections of the future as well as in observed trends. However, it has been found that local (sub-)hourly precipitation extremes could be much more sensitive to warming with higher apparent scaling than the CC scaling. For example, Lenderink and van Meijgaard (2008) found that one-hour precipitation rates increase twice as fast with rising temperatures as expected. This so-called super CC scaling has received considerable attention in the scientific literature over the last 10 years. Despite this, its cause is still unsettled.

To understand extreme precipitation scaling better, knowledge of both the shape and evolution of the associated winds is crucial. In this thesis, the hypothesis which states that feedbacks from the local cloud dynamics are responsible for the super CC scaling is adopted. These dynamics are studied by considering the vertical wind velocities, which play a key role in rain formation by transporting moisture upward in the clouds.

In order to study the intensification of convective precipitation, very detailed model simulations with a Large Eddy Simulation have been performed for an idealized composite of typical conditions with heavy rain in the Netherlands. By systematically perturbing the starting atmospheric temperature under constant relative humidity conditions, a strong response of cloud dynamics to warming has been found by Lochbihler et al., 2019. The processes driving these enhanced cloud dynamics are of interest. In this research it is further investigated how moisture transport into extremely precipitating clouds is affected by a changing climate.

1.2. Research aim

The research aim is to determine and quantify the importance of dynamic processes that contribute to the scaling of extreme precipitation in mid-latitudes. This scaling is stronger than the (well-known) CC scaling for sub-daily timescales. This aim will help to better understand how extreme precipitation in the Netherlands will intensify in a warmer climate.

1.3. Background

To understand the research questions and hypotheses, the reader should know a few high level concepts. More background can be found with accompanying literature in Chapter 2. For the sake of introducing the research questions and hypotheses in Sections 1.4 and 1.5, they are already stated here.

First, extreme precipitation on (sub-)hourly timescales comes from convective clouds. The thunderstorm cloud or cumulonimbus is a prime example of this. From these clouds, the precipitation rate may be related to amount of moisture in the clouds. This is expressed with the total specific humidity in the cloud $q_{t,c}$. Furthermore, the speed at which moisture is transported up in the cloud w_c is determining. This is expressed with Equation 1.1.

$$P_r \sim w_c q_{t,c} \tag{1.1}$$

Cold-pools are introduced. By the American Meteorological Society (AMS) they are defined as "a region or 'pool' of relatively cold air surrounded by warmer air" (Glickman & Zenk, 2000). Cold-pools are relevant because they are denser than their surroundings, and thus spread out horizontally if they are constrained near the surface of the earth from descending. This drives gust fronts at their edges which ultimately might enhance extreme precipitation.

1.4. Research questions

The objective of this research is to understand more about idealized extreme precipitation events in a warming climate in the Netherlands. Therefore, the main research question is formulated as follows:

How do dynamic processes enhance extreme precipitation intensification in a warming climate in the Netherlands?

The main research question is divided into three sub-questions. From these questions, A and B are related to processes in the clouds themselves. Question C is focused on how organization in the sub-cloud layer by so-called cold-pools feeds back, resulting in more intense precipitation. The concept of what a cold-pool is, is explained in Section 2.3.

In a warming atmosphere over the Netherlands...

    A *... how are updrafts in the clouds changing?*
    B *... how is the moisture transportation into the clouds changing?*
    C *... what is the influence of cold-pool associated sub-cloud gust fronts on updrafts in the clouds?*

1.5. Hypotheses

Hypotheses are formulated on the basis of an assumption of constant relative humidity. This means that with increasing temperature, the absolute humidity increases. Increasing temperature is increasing the moisture content of the atmosphere.

The updraft velocities in convective clouds increase with increasing temperature.

This can be viewed from a budget perspective. With increased moisture, more of the moisture can be converted from water vapor to condensed water in the clouds. This releases more heat into the air, making updrafts more buoyant. The updrafts will thus accelerate more.

Cold pools provide a positive feedback loop to the increase of precipitation with increasing temperature.

Increased precipitation rates in a warmer climate create stronger downdrafts due to increased evaporation rates. These downdrafts hit the surface and spread out laterally into cold-pools. At the edges of the cold-pools this spreading out creates an abundance of air, called convergence. The converging air enhances updrafts below the clouds. These enhanced updrafts transport moisture into the clouds. This conceptual loop is shown in Figure 1.1.
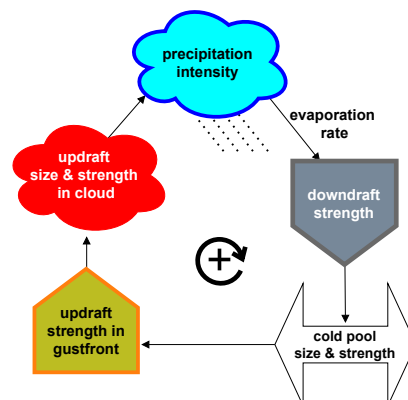
Figure 1.1: Feedback loop of dynamical processes leading to stronger than Clausius-Clapeyron scaling of extreme precipitation.

1.6. Knowledge gap

High resolution numerical simulations used to study dynamics of extreme precipitation in an idealized future climate in the mid-latitudes is a topic that is not fully covered yet. The previous statement is broken down over the following paragraphs to show how this work covers a unique niche.

High resolution model simulations

Numerical simulations with Cloud Resolving Models have been used in literature to study deep convection. The usage of the more detailed Large Eddy Simulations is more rare. Besides, the mid-latitudes are the region studied here. The mid-latitudes are not so well studied as the tropics.

The region studied

The Radiative-Convective Equilibrium (RCE) assumption does not hold for the mid-latitudes in contrast to existing work studying the tropics. This work builds directly on the work done by Lochbihler et al. (2019). In other simultaneous work, Lochbihler et al. (2021) analyze a bigger set of climate perturbations than what is used in this work, concluding that cold-pool dynamics shape the response of precipitation intensities. What is novel in this work is that the dynamics of updrafts are investigated and the climate scaling of their contributions is directly considered.

The difference from closely related work

In Loriaux et al. (2013) dynamics are considered in a simple entraining plume model. On the other side, the work by Lochbihler defines the boundary of the novelty of this work. How this work fits between is shown in Figure 1.2. The knowledge gap filled is in between the work of Loriaux and Lochbihler. Here, Large Eddy Simulation simulations are used to quantify the change of dynamics in the clouds and the sub-cloud layer.
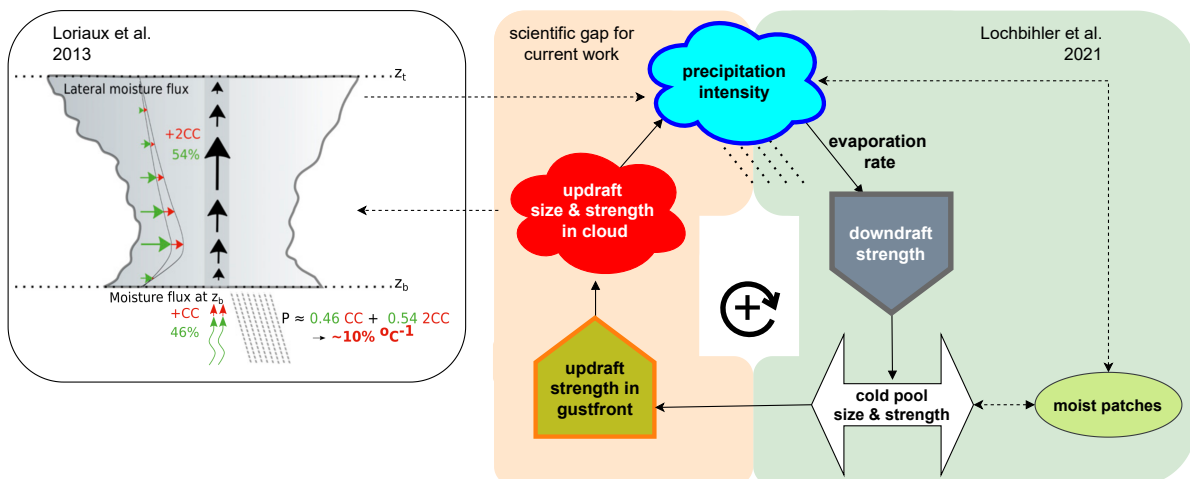
Figure 1.2: Novelty of this work in relation to previous research by Loriaux et al. (2013) on an entraining plume model and Lochbihler et al. (2021). whom related cold pools, precipitation intensity and so-called 'moist patches'

1.7. The approach outlined

The effects of climate change can be simulated in a model by using measurements of the atmosphere in the current climate during current extreme precipitation events. These measurements can be used to construct a vertical temperature profile. This profile is put into a model to find the precipitation in a reference case. The input profile can be made warmer or colder. This is called a perturbation. The sensitivity of extreme precipitation to climate change can be investigated by comparing perturbed climate simulations with the reference simulation. A catalog of extreme precipitation events from 1995 to 2014 in the Netherlands was made by Lenderink et al. (2017). An idealized composite of these conditions was used in Lochbihler et al. (2019) to simulate a day with extreme precipitation in the Dutch Atmospheric Large Eddy Simulation (DALES).

In Chapter 2, definitions (e.g. what precipitation scaling is) are given from literature. The concept of how 'cold-pools' can intensify precipitation is given in Figure 2.6.

The idealized extreme precipitation day was also simulated with perturbed temperature height profiles to mimic climate change. This was done for climate scenarios with warming and cooling. Relative Humidity is assumed constant. The outputs of these detailed simulations are described in Chapter 3.

In the methods in Chapter 4, it is described how the large amount of data in the simulation outputs is treated. Numerical noise is removed by filtering and a period in the simulation day similar to Lochbihler et al. (2019) is selected for detailed analysis.

The results Chapter 5 follows after that. The topics of the results go from updrafts in the clouds to downdrafts. Followed by the cold-pools near the surface back up to the buoyant acceleration in the clouds. After this a more three-dimensional picture is sketched and grid points are linked in vertical columns. Finally, the effects of warming on moisture transport are quantified.

The discussion, conclusion and recommendations of this work can be found in Chapter 6.

2

Theoretical introduction

The goal of this chapter is to gain a deeper understanding of what is already known in literature about how updraft related processes drive extreme precipitation in mid-latitudes. An explanation of how the scaling of precipitation intensity with dew point temperature increase works is given in Section 2.1 after which a split into defining contributions for the scaling is made in Section 2.1.7. Next a conceptual model is used to show how super-CC scaling is driven by moisture flux into the cloud through the cloud base and the sides in Section 2.2. Such an entraining plume model, doesn't capture the effect of cold-pools on atmospheric dynamics though. Cold-pools dynamics are reviewed in Section 2.3. The reason for using Large Eddy Simulations and some of modeling results over the tropics are treated in Section 2.4.

This chapter answers the following questions:

- How is precipitation intensity scaling defined?
- What are cold-pools and how are their size and strength changing?

2.1. Scaling of precipitation

In this section, first the relative humidity is introduced. This is a metric that might be familiar even to readers without a background in atmospheric science. Next, the step to the Clausius Clapeyron (CC) relation is made. The CC relation leads to more extreme precipitation with temperature. Next, it is motivated why dew point temperature is a better metric for measuring apparent scaling extreme precipitation relations in Section 2.1.3

2.1.1. Relative humidity

Relative Humidity (RH) is the fraction of absolute humidity over the humidity at which saturation occurs. The RH is often expressed as a percentage. At $RH = 100\%$, the air can not hold any more water vapor and excess water condenses. (Supersaturation is ignored here for simplicity.)

The definition of $Relative Humidity$ is given in Equation 2.1. The CC relation governs the saturation specific humidity, q_{sat}, as a function of temperature, T, and pressure, p. Or equivalently it governs the saturation pressure, e_{sat} of the air as a function of temperature.

$$RH = \frac{q_v}{q_{sat}(T,p)} = \frac{e_v}{e_{sat}(T)} \tag{2.1}$$

The relative humidity is the fraction of the water vapor specific humidity q_v over the q_{sat}. These are both mass ratios, but equivalently a pressure ratio can be used between the vapor pressure e_v over e_{sat}. The e_{sat} can be calculated with the integrated CC relation, which is given in Section 2.1.2 hereafter.

2.1.2. The Clausius-Clapeyron Equation

In a future climate, which is expected to be on the order of degrees warmer, precipitation extremes are expected to increase. With warming of the environment, an increase of extreme precipitation with (dew point) temperature can be found. On larger spatial and longer temporal scales, the amplification of rainfall with temperature, often follows from the Clausius Clapeyron (CC) relation.

The CC relation is given in Equation 2.2. The derivation from fundamental thermodynamics, with accompanying assumptions, is given in literature (e.g. North & Erukhimova, 2009; Wang, 2013).

$$\frac{de_{sat}}{dT} = \frac{e_{sat}L_v}{RT^2}$$

(2.2)

The CC equation describes the change of saturation vapor pressure, e_{sat}, with temperature T as other variables are the latent heat of condensation, L_v and the gas constant for water vapor, $R = 461 J kg^{-1} K^{-1}$. It can be rewritten as to find the saturation vapor pressure with Equation 2.3. This rewriting entails separating variables, integrating and assuming that L_v is constant with temperature at $2.5 * 10^6 J kg^{-1}$.

$$e_{sat} = e_0 * e^{\frac{L_v}{R_v} * (\frac{1}{T_0} - \frac{1}{T})}$$

(2.3)

In this integrated form of the CC equation, the reference pressure, e_0, and reference temperature T_0 can be set to 611 hPa and 273 K respectively. Using set constants, the CC scaling rate can be found. This gives near the earth's surface an increase of q_{sat} of 6-7% per degree warming. Under the assumption of constant RH, the actual water vapor in the air near the surface will also follow the same dependency of 6-7 % per degree. In the introduction of Lenderink and Attema (2015), papers showing this are discussed.

The assumption of unchanged relative humidity is reasonably well satisfied in projections of future climate. Therefore, the increase in humidity of the air in the warmer future climate is reasonably well predicted by the CC relation. It is expected that rainfall intensities will increase proportionally to the increase in absolute humidity, giving rise to an increase in precipitation extremes which follows the CC relation.

2.1.3. Using dew point temperature for scaling

Dew point temperature, T_d is the temperature to which a given air parcel must be cooled at constant pressure and constant water vapor content in order for saturation to occur. This definition of dew point temperature is given in Equation 2.4. It means that if a parcel reaches its dew point temperature, relative humidity will be 100%. Under constant relative humidity, dew point perturbations are the same as temperature perturbations. (Lenderink & Attema, 2015)

$$q_v = q_{sat}(T_d, p)$$

(2.4)

Dew point temperature is primarily a measure of humidity at a certain temperature and pressure, why should the apparent scaling of extreme precipitation with climate change (Temperature) be complicated by using dew point temperature?

In literature it has been extensively motivated why the intuitive temperature apparent scaling should be replaced by dew point temperature. For example, Chan et al. (2015) demonstrate the pitfalls of using surface temperature as an apparent scaling variable. One example of such pitfalls is a large scale synoptic scale low pressure, which is associated with reduced temperature and increased precipitation. Synoptic scale conditions affect both temperature and precipitation at the same time (Bao et al., 2017). Consequently, the dependency of hourly precipitation extremes to dew point has a more robust apparent scaling behaviour and it is therefore preferred to use scaling with dew point temperature rather than scaling with temperature (Lenderink & van Meijgaard, 2010).

Scaling is the dependency of precipitation extremes to (dew point) temperature. These dependencies for daily, hourly and per 10 minute precipitation extremes on dew point temperature are derived from present-day climate by pairing measurements of these quantities. Dividing the data into bins based on dew point temperature gives scaling relations. The extreme precipitation cases are selected by only taking a scaling relation at high percentiles. An example of such results is shown in Figure 2.1.
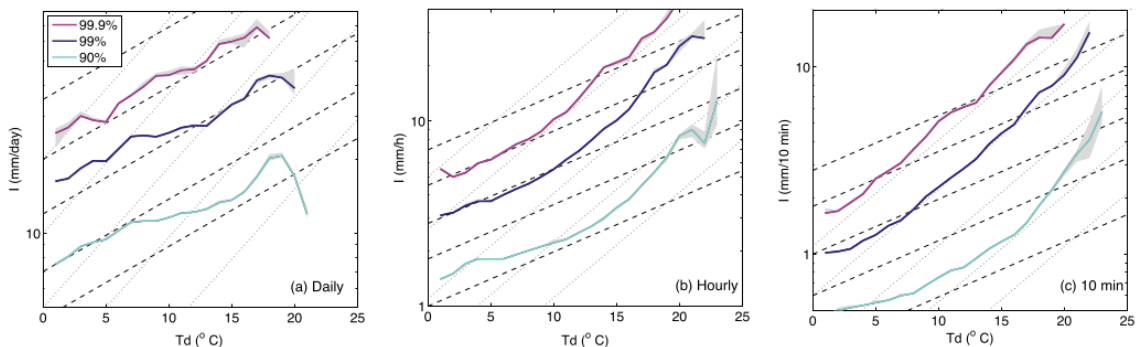
Figure 2.1: Observed precipitation intensity over the Netherlands for the 90th, 99th, and 99.9th percentiles, with respect to dew point temperature at daily, hourly, and 10-min resolution. Gray shading indicates the 95% confidence interval. Dashed lines indicate a CC intensity increase, while dotted lines indicate a 2CC increase. Adapted from (Loriaux et al., 2013)

2.1.4. Super Clausius-Clapeyron scaling

On shorter timescales, such as precipitation per hour or 10 minutes, the apparent scaling of extreme precipitation with warming can exceed the CC-scaling by up to double apparent scaling. (Lenderink & van Meijgaard, 2008; Lochbihler et al., 2019) This super CC apparent scaling in mid-latitudes has implications for the design of urban drainage. It means a higher Probable Maximum Precipitation PMP, which is frequently used as a design parameter for critical infrastructure. The derivation of PMP is typically based on a simple CC scaling assumption, but Singleton and Toumi (2012) argues for a PMP using the double of CC scaling.

2.1.5. Timescale for scaling relations

Precipitation can be viewed on several timespans and spatial domains. Under the assumption that the same amount of water is removed from the atmosphere, the amount is always a trade-off between spatial coverage, intensity and duration or temporal frequency (Trenberth et al., 2003). A choice is made to work with a 10 minute timescale in the next paragraph.

In climate model predictions, precipitation extremes are given per hour. For comparison with these predictions an hourly precipitation rate would be beneficial (Trenberth et al., 2003). However, the hourly intensities smooth out the precipitation extremes (e.g. Singleton & Toumi, 2012). Therefore, sub-hourly timescales are relevant for the investigation of peak intensity. In this work the 10 minute timescale is adopted similar to Loriaux et al. (2013), where higher temporal resolutions showed stronger climate scaling rates already at lower dew point temperatures. This is in accordance with a typical minimal timescale for Probable Maximum Precipitation, used for urban drainage design.

2.1.6. Precipitation in an extreme event

An extreme event does not have a set amount threshold, but means that the event rarely occurs. What is extreme in one location is not necessarily extreme in another location. Therefore using only the highest percentiles of the amount of rain when it rains give a measure of extremity. The higher the percentile, the rarer the event and thus the more 'extreme'.

The amount of precipitation in the convective showers of interest is determined by the amount of condensed moisture in the cloud that it's coming from and how much of it reaches the ground. This water arrives in the cloud being carried skyward in updrafts. In an extreme event on short timescales (e.g. hourly), the precipitation is of convective nature. For such an event, it may be assumed that moisture is transported vertically whilst all moisture in excess of the saturation specific humidity is condensing in the cloud. This happens from cloud base to cloud top according the lapse rate of condensation, $\frac{\partial q_{sat}}{\partial z}$ and the mass of air being displaced with density ρ and vertical velocity w. Not all moisture transported into the cloud ultimately reaches the surface as precipitation, this is captured with the precipitation efficiency, ε.

Using the definitions stated in Section 2.1.6, the simplified Equation 2.5 can be formulated similar to a volume of literature (e.g. Abbott et al., 2020; Loriaux et al., 2017; Muller & Takayabu, 2020). In Appendix C it is derived in accordance with Muller et al. (2011).

$$P_e = \varepsilon \int_{surf}^{trop} \rho w \left(-\frac{\partial q_{sat}}{\partial z}\right) dz \qquad (2.5)$$

2.1.7. Scaling contributions

Scaling all quantities in 2.5 with the rate of change, δ, divided by the orignal quantity gives the fractional scaling. The contributions to the fractional scaling of precipitation by the components on the right hand side of Equation can be separated. For this research, the focus is on the dynamic contribution, yet background knowledge on the other contributions is relevant. The first order contributions can be split into three parts; the thermodynamic, dynamic and microphysics contribution (Muller & Takayabu, 2020). This is shown in Equation 2.6. The limits of integration are dropped here for brevity.

$$\underbrace{\frac{\delta P_e}{P_e}}_{\text{precipitation scaling}} = \underbrace{\frac{\delta \varepsilon}{\varepsilon}}_{\text{microphysics}} + \underbrace{\frac{\int \delta(\rho w) * (-\frac{\partial q_{sat}}{\partial z}) dz}{\int \rho w (-\frac{\partial q_{sat}}{\partial z}) dz}}_{\text{dynamic}} + \underbrace{\frac{\int \rho w * \delta(-\frac{\partial q_{sat}}{\partial z}) dz}{\int \rho w (-\frac{\partial q_{sat}}{\partial z}) dz}}_{\text{thermodynamic}} \qquad (2.6)$$

Thermodynamic scaling contribution

The increase in moisture convergence results directly from increases in moisture content of the air, this is the thermodynamic contribution, which relates the amount of water vapor available in the atmosphere to the amount of precipitation that will fall onto the surface. Relative humidity is expected to change little with warming, thus absolute humidity increases with temperature according to the CC relation of about $6 - 7\%$ per degree of warming. The thermodynamic contribution therefore refers directly to the increase in moisture content moving into a cloud assuming that the motions (second right hand term in Equation 2.6) do not change.

Dynamic scaling contribution

Changing velocity fields enhance the moisture convergence. This term, related to the increase in dynamics, is what's called the dynamic contribution. This dynamic contribution relates the vertical mass flux in updrafts to the amount of moisture transported into the clouds (Muller & Takayabu, 2020).

Besides moisture being transported from the bottom, moisture convergence from the sides increases by increased horizontal inflow into the clouds also plays a role (Loriaux et al., 2013). The dynamic contribution causes the scaling of precipitation to exceed the CC-scaling rate and is a source of uncertainty to how much stronger precipitation extremes will be in a future climate (Pendergrass, 2020).

Microphysics scaling contribution

Besides the dynamic and thermodynamic contributions, the precipitation scales through how efficiently the transported moisture is converted into precipitation (Loriaux et al., 2013). Cloud microphysics precipitation efficiency is defined as the fraction of condensation in a convective updraft which eventually falls down and reaches the surface as precipitation (Sui et al., 2007). It is typically less than one as some of the condensates evaporate as they fall down into warmer air below (Muller & Takayabu, 2020). This is determined by the microphysics contribution. Phase changes of water happen at a molecular scale, these are processes that are to fine to replicate in a model. So microphysics are parameterized in Large Eddy Simulations. Changes in the microphysics contribution are not considered in this study.

2.2. Understanding super-CC scaling with an entraining plume

The importance of the thermodynamic- and dynamic contributions to precipitation scaling can be shown with a simple entraining plume model. This model describes a column of air rising from the surface and can for example be found in parameterized models like Numerical Weather Prediction (NWP) models.

2.2.1. Formulation of the entraining plume model

In the entraining plume model, the thermodynamic state is solved in an upward loop until the vertical velocity becomes zero at the cloud top. The bulk plume model can be formulated as in Loriaux et al. (2013) in three budget equations for a steady state.

The first, Equation 2.7, is the budget of dry static energy, $s = C_p T + gz$. The second, Equation 2.8, is the water vapor specific humidity, q_v, budget. And the third, Equation 2.9 is the cloud water specific humidity q_c budget. For this formulation the total specific humidity is $q_t = q_l + q_v$. Ice is neglected here.

$$w_{cld}\frac{\partial s_{cld}}{\partial z} = -L_v c - \epsilon w_{cld}(s_{cld} - s_{env}) \tag{2.7}$$

$$w_{cld}\frac{\partial q_{v,cld}}{\partial z} = -c - \epsilon w_{cld}(q_{v,cld} - q_{v,env}) \tag{2.8}$$

$$w_{cld}\frac{\partial q_{l,cld}}{\partial z} = c - G - \epsilon w_{cld}q_{l,cld} \tag{2.9}$$

In the formulation of the entraining plume, w is the vertical velocity, G is the autoconversion from cloud condensed water to precipitation, ϵ is the lateral entrainment rate of environmental air into the cloud and the subscripts cld and env are representing in-cloud and environmental values respectively.

Using the plume model, precipitation formation can be understood from considering the total moisture budget in the cloud column. In Loriaux et al. (2013), this moisture budget for a steady state in the cloud is formulated as in Equation 2.10.

$$w_{cld}\frac{\partial q_{t,cld}}{\partial z} = -G - \epsilon w_{cld}(q_{t,cld} - q_{t,env}) \tag{2.10}$$

Assuming no evaporation of rain, the surface precipitation rate P_e is related to the autoconversion rate in Equation 2.11.

$$P_e = \int_{z_b}^{z_t} \rho G dz \tag{2.11}$$

In Equation 2.11, P is calculated as the integration of the in-cloud density (ρ) weighted autoconversion. The limits are from cloud base, z_b to cloud top, z_t

Under the assumption that the maximum amount of precipitation that can fall out of an atmospheric column is determined by the total amount of condensation in the column, the precipitation intensity relates directly to the condensation rate. This assumption has the implications that the q_c is zero and G is equal to the condensation rate. Since $q_c = 0$, $q_{t,cld} = q_{sat,cld}$. This allows for the solving of the precipitation rate with by changing Equation 2.8 into 2.12.

$$P_e = -\int_{z_b}^{z_t} \rho * w_{cld} * \left(\frac{\partial q_{sat,cld}}{\partial z} + \epsilon(q_{t,cld} - q_{t,env})\right) \tag{2.12}$$

2.2.2. Super CC scaling in an entraining plume model

The entraining plume model and the resulting moisture fluxes into the cloud are illustrated in Figure 2.2. A cloud updraft is depicted as the darker grey column, with the arrows indicating updraft speed. Here, it is assumed that in the end moisture convergence leads to precipitation formation. Moisture enters this column at cloud base and sideways into the cloud.

In the model, precipitation intensity increase is greater than the thermodynamic component, CC climate scaling. This super CC climate scaling is controlled by a flux of moisture through the cloud base and lateral moisture convergence. In Figure 2.2 these contributions are shown for an idealized deep convective case over the Netherlands (Loriaux et al., 2013). The cartoon has been simplified to show positive lateral flux throughout the cloud column.
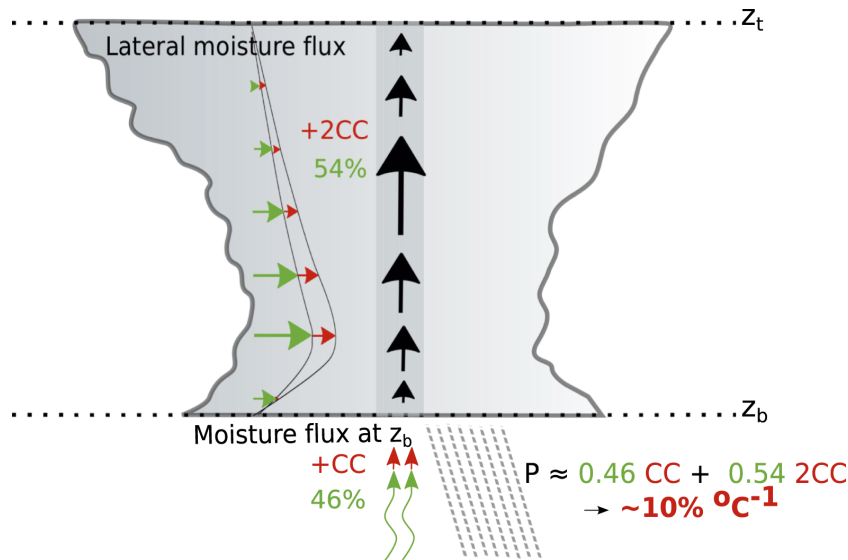
Figure 2.2: Cartoon illustrating how precipitation intensity climate scaling as found from an entraining plume model is built up from lateral and cloud-base moisture fluxes. Green is used to indicate the initial state, while climate scaling per degree of warming is depicted in red. (Loriaux et al., 2013)

The climate is perturbed by making the input profile warmer or colder. The influx of moisture at cloud base has CC climate scaling because it is only controlled by the thermodynamic component in the entraining plume model. This CC climate scaling of the thermodynamic term was already described in Section 2.1.7. The dynamic component is associated with the strength of the upward motions in the cloud. The strength of these updrafts is (largely) determined by latent heat release. More available

moisture leads to more condensation and therefore increased latent heat release, which leads to stronger cloud updrafts (Lenderink & van Meijgaard, 2010). This promotes extra moist air being sucked in from the sides, which compounds with the thermodynamic CC scaling to lead to double CC climate scaling of the laterally entrained moisture. This lateral entrainment is an additional contribution compared to the three scaling contributions in Equation 2.6. In Loriaux et al. (2013), the relative importance of the climate scaling of the lateral and cloud-base moisture fluxes was found to be indicated in the green numbers. The resulting proposed climate scaling of extreme precipitation was 10% per degree Kelvin (Celsius) of warming.

2.2.3. Limitation of the entraining plume compared to LES

A limitation of the entraining plume model is that environmental conditions are fixed to a steady state. It does not incorporate processes that affect these conditions such as feedback effects from cold-pools on the sub-cloud updrafts (Loriaux et al., 2013). This means that updrafts near the surface do not change with climate perturbations as no condensation happens below the cloud. The atmospheric temperature and humidity profiles are set and can not be influenced by the transport of heat and moisture upwards which does happen in reality.

2.3. Cold-pools

The reader can get some familiar with how cold-pools look with a oblique view in Figure 2.3a and a view from space in Figure 2.3b. In the latter Figure, the rings of clouds near the edges of the cold-pools can be associated with the so-called gust front. These pictures are not from the mid-latitudes and are meant to create intuition for how cold-pools modulate the organisation of clouds conceptually.

(a) Picture taken from an aircraft on August 25, 2016, southeast of Barbados. Noteworthy are the cloud lines to the left of the image, with the nearby cold-pool convection organized in a circle, a portion of which is oriented perpendicular to the cloud lines in the left-hand side. Isolated convection reaching a higher altitude is detraining, most likely into a layer of increased stability
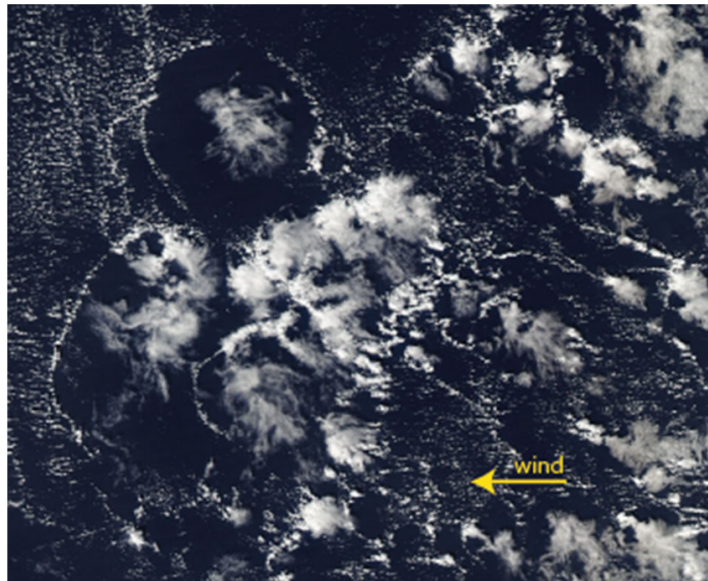
(b) December 19, 2013, MODIS AQUA satellite 13:30 pm LT visible image, east of Barbados (46.5–50° W, 17.5–20° N). The wind is flowing from right to left. The two largest cold-pools span approximately 100 km and are better defined on the downwind side, particularly the left side of the image. The higher cloud tops within the cold pool centers reach approximately 4 km

Figure 2.3: Examples of cold-pools near Barbados from Zuidema et al. (2017)

2.3.1. Cold-pool dynamics

Due to their negative temperature perturbation, cold-pools get their name. Cold-pools are generated as precipitation falls from a convective cloud. As it reaches lower layers, it evaporates and transfers momentum through the liquid water loading on the air it travels through. The evaporation of precipitation

causes the air to become negatively buoyant. Negatively buoyant air descends and reaches the surface. Air lower in the boundary layer is generally moister, so the descending air will be relatively cold and dry (Tompkins, 2001). An illustration of representation of cold-pools in a simple model is shown in Figure 2.4

(a)   **(b)**
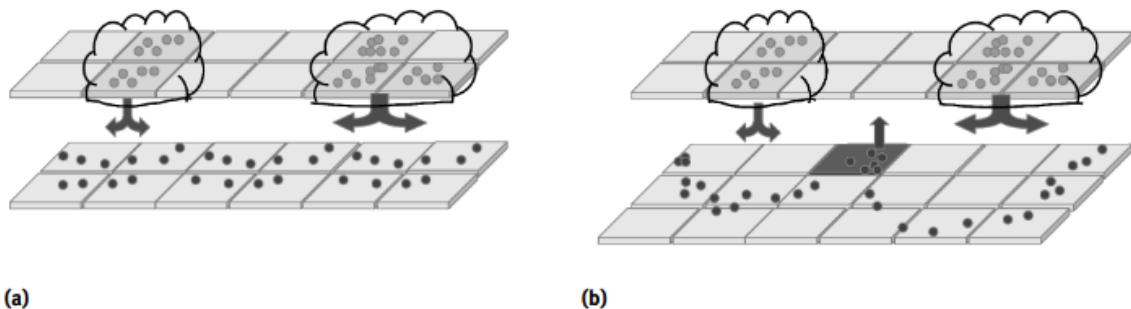
Figure 2.4: Illustration from Böing (2016) of a representation of cold-pools in a simple particle model. This model is not based on physics, but mimics how grains of sand roll down when they are released onto a sandpile. The particles here are representing instability and convergence. The particles form downdrafts in a) where convergence of air into the clouds acts on the lower layer, causing divergence, which leads to b) triggering of new convective cells somewhere else

Near the edges of the cold-pools, a gust front travels outward (Fournier & Haerter, 2019). New storm cells can be generated due to the updrafts and/or the increased moisture around these edges. This organization of convection as a result of cold-pool dynamics might be a defining factor in making the scaling of extreme precipitation super-CC (Haerter & Schlemmer, 2018). Horizontal heterogeneity in wind fields and thermodynamic variables due to Cold-pool dynamics are not captured by the entraining plume model from Section 2.2. Therefore, a modelling approach where cold-pool dynamics can be resolved is essential for understanding climate scaling of extreme precipitaion.

Convective self-aggregation is when (thunderstorm) clouds cluster. Whether numerical simulations succeed (e.g. Haerter, 2019) or fail at producing this organization depends on modeling choices. A degree of organization can point to stronger processes transporting mass, momentum, moisture and heat which can invigorate updrafts, increase cloud sizes and enhance the resulting extreme precipitation. (Pendergrass, 2020)

Feng et al. (2015) examine the mechanisms of convective cloud organization by cold-pools in a warm tropical oceanic environment, replicating observations with a model. They schematically show how intersecting cold-pools trigger more convection with enhanced updrafts. Furthermore, they showed that clouds triggered by cold-pools can grow to be deep clouds due to stronger organization. This is illustrated in Figure 2.5

Different types and sizes of cold-pools exist. For the application in this research, the definition is limited to mesoscale convective system cold-pools. The cold-pools are a type of organization that can not be resolved in course grid models and therefore Large Eddy Simulations can be used to study their relation to extreme precipitation scaling (Pendergrass, 2020).

2.3.2. Feedback loop in the sub-cloud layer

The hypothesis that cold-pools promote feedback on precipitation intensification is made explicit here and supported by literature. After that, the feedback is repeated in a step by step list.

Deep convection and extreme precipitation can be related to a feedback loop in the sub-cloud layer. Cold-pools spread out over the surface after the descending relatively cold, dry air reaches the surface through density currents driven by mass continuity. They change the dynamic and thermodynamic properties in the sub-cloud layer. This is associated with wider cloud widths and heights. A cloud can be seen as a pyramid in a simplistic view, with a wider base it can be higher. These bigger clouds then precipitate more, leading to more evaporation and thus stronger cold-pool dynamics. (Böing, Steven
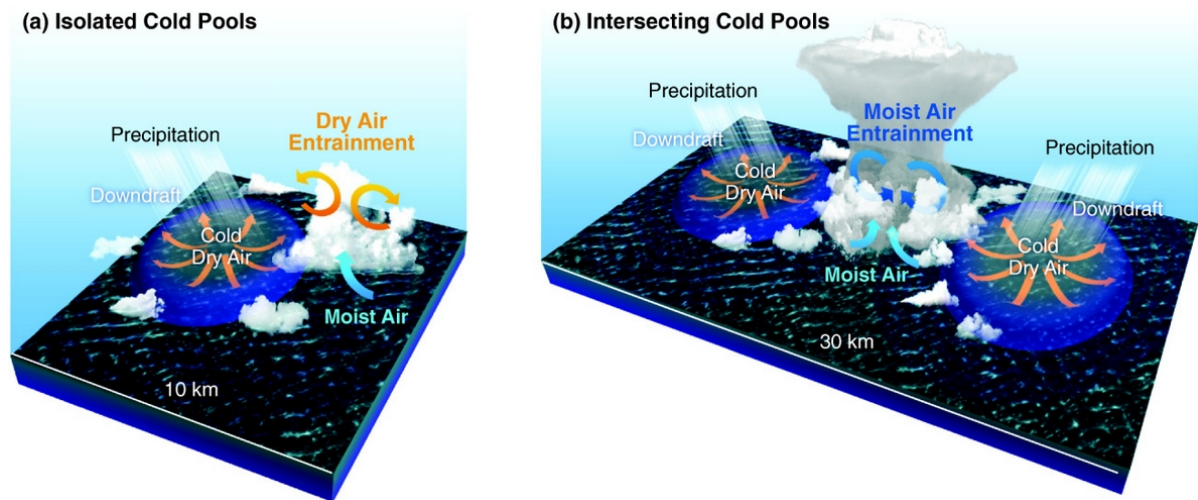
Figure 2.5: Schematic from Feng et al. (2015) of the mechanism of convective organization by cold-pools. For isolated cold pools (a), moist air at cold pool edges are lifted up by the downdraft-induced outflow and trigger new convective clouds, but entrainment of relatively drier environment air above the boundary layer oftentimes limit the vertical growth. For intersecting cold pools (b), more clouds are triggered at their intersecting boundaries and the distance between clouds is reduced, creating larger cloud clusters. As a result, entrainment is limited within the nearby moist cloudy air, favoring the growth of the new clouds into deep convection.

et al., 2012)

Near the edges of cold-pools, new storm cells can be generated due to the updrafts and/or the increased moisture. Cold-pools act like conveyor belts transporting moisture and momentum over a large area. If this momentum and moisture is confined into a small area, it has to go somewhere. Due to mass and momentum continuity, converges and escapes upward. This low level convergence happens near the cold-pool boundaries. Near these boundaries strong winds are flowing radially outwards and upwards in what is called a gust front. The convergence near the cold-pool edge removes convective inhibition and ultimately promotes deep convection (Fuglestvedt & Haerter, 2020). When multiple (2 or 3) cold-pools collide, the convergence higher up sets the stage even more favorable for deep convection as is explained in more detail in Meyer and Haerter (2020).

Based on the works of Haerter and Schlemmer (2018), Lochbihler et al. (2021) and Lochbihler et al. (2019), a feedback loop for uniform atmospheric dew point temperature increase was formulated for Bentvelsen et al. (2021) and shown in Figure 2.6. This feedback loop summarizes how cold-pool related dynamical processes amplify precipitation scaling. It was previously shown in Figure 1.1.

So what happens to precipitation with warming due to cold-pools?

- The atmosphere holds more moisture.
- Precipitation becomes more intense.
- As the more intense precipitation falls, it cools downdrafts by evaporating.
- The cooled downdrafts are more dense.
- The air spreads out near the surface more and faster because of larger density differences with the environment. In other words, the produced cold-pools are stronger.
- The stronger cold-pools have more convergence at the outflow boundaries.
- Gust fronts near the outflow boundary have stronger updrafts.
- Updrafts in the clouds accelerate more due to increased latent heat conversion.
- Stronger cloud updrafts promote the intensification of precipitation. This closes the feedback loop.
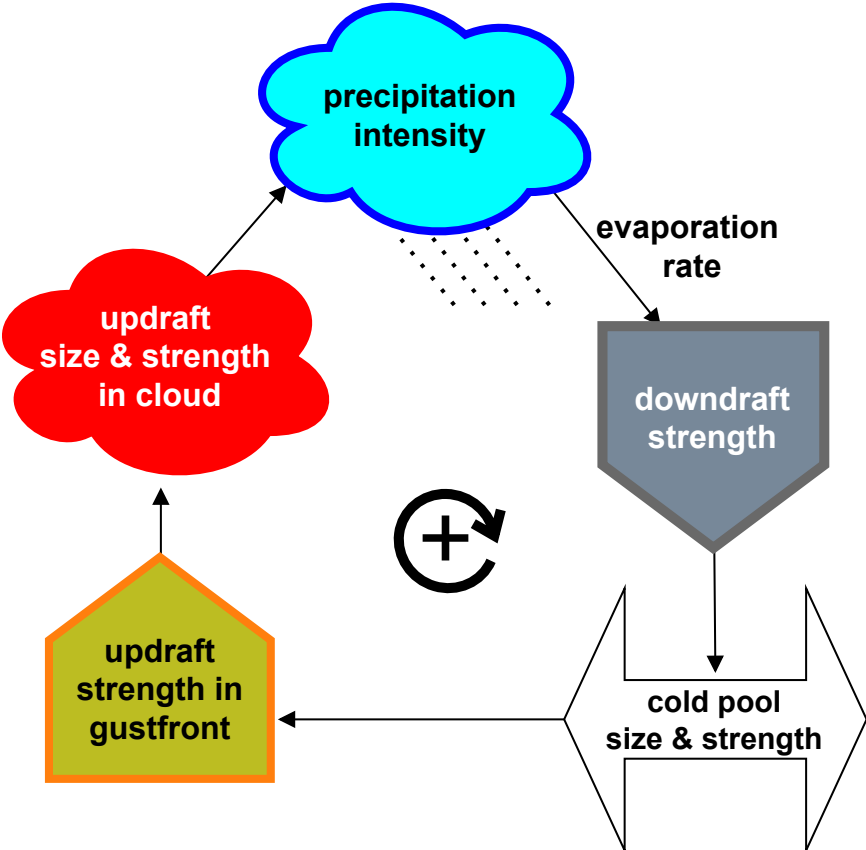
Figure 2.6: Feedback loop of dynamical processes leading to stronger than Clausius-Clapeyron scaling of extreme precipitation. This figure was part of a scientific presentation and is reproduced with authorization (Bentvelsen et al., 2021)

2.4. The choice for Large Eddy Simulations

To study the dynamical processes in a convective cloud, very high resolution is needed, so that turbulent motions are well resolved. A tool to do this is called Large Eddy Simulation. LES models are similar to Cloud Resolving Models CRM, but have a higher resolution that enables resolving the eddies containing most of the energy ($\sim 90\%$). They do this by solving the budget equations for filtered variables including momentum and thermodynamic state variables, such as heat, entropy, or the total water specific humidity (Heus et al., 2010). To resolve the eddies in LES, high spatial resolution is required with short timesteps. So why can't extreme precipitation be researched well with computationally less expensive models? The answer to that question is in the next paragraph.

Models such as Numerical Weather Prediction (NWP) or climate models do not resolve clouds, but use parametrization schemes to represent cloud processes instead. This makes them computationally cheaper. Problems are that these models have known issues in the timing of onset of precipitation in the diurnal cycle. One can think of the balance between spatial coverage, intensity and duration. Besides the precipitation starting and peaking too early, the parameterized models also have difficulty representing the intenser events often occurring later on the day. LES can be used to study the diurnal cycle in more detail, potentially leading to better parameterizations of extreme precipitation. However, the biases of convection parameterization schemes can not be resolved by a choice of better parameterization criteria to activate deep convection alone. The problem partly also lies in the representation of a succession of regimes from dry convection to precipitating convection, another reason to prefer LES. (Guichard et al., 2004)

Besides modelling, observations might be used to extrapolate trends. Observations might show a dependency of extreme precipitation to dew point temperature variations in the current climate. Estimating the increase from observations is called apparent scaling Lenderink et al., 2021. A useful approach that does however pose a problem. Parameterizations in climate models are not necessarily the same for the current climate as for a future climate (Muller & Takayabu, 2020). Therefore a deeper understanding of the underlying dynamics and thus the role of updrafts on precipitation scaling can ultimately improve forecasts and LES is the tool to use for it.

2.4.1. Previous modeling results

A volume of literature describing the scaling over the tropics and over sea using CRMs is available. Pendergrass (2020) and Muller and Takayabu (2020) give reviews of this. Mrowiec et al. (2012) compares updraft and downdraft properties in some CRMs during an observed strong convective event in tropical Australia.

The changes in the dynamic scaling contribution due to updrafts is important, since in the tropics it can lead to a negative dynamic component due to a changing vertical profile as found by Muller et al. (2011). Therefore understanding the profile of the vertical velocity with height is required to understand extreme precipitation scaling.

In the tropics assuming Radiative-Convective Equilibrium (RCE) for the energy budget is valid. In mid-latitudes however, RCE does not hold since energy is transported into the domain by synoptic scale flow. This work is aimed at the Netherlands, which is in the mid-latitudes. The mechanisms behind scaling of precipitation in these extra-tropical regions are less well studied using LES.

3

Case description

In this Chapter, first an overview is given of how the COLD, REF and WARM scenarios are constructed in Section 3.1. Temperature and moisture profiles of the three simulations are given. In Section 3.2, relevant initial and boundary conditions are given. After that, the output variables are described in Section 3.3

Available are outputs of the Dutch Atmospheric Large Eddy Simulation (DALES) model of an idealized extreme precipitation day. The boundary and initial conditions are constructed from a composite of the 10% most extreme precipitating events from 1995 to 2014 observed in the Netherlands (Loriaux et al., 2016). These input conditions are further idealized and used in Lochbihler et al. (2019) to simulate one day with extreme precipitation. In this work, those outputs are scrutinized.

3.1. Climate simulations

The reference simulation (REF) is constructed from a catalogue of atmospheric profiles from days with extreme precipitation. These atmospheric profiles are combined to find an idealized profile of temperature with height as input for DALES.

Changed climates are simulated by perturbing the vertical temperature profile of the atmosphere by a constant amount compared to the reference scenario. The relative humidity is set to be constant, so temperature perturbation is the same as dew point temperature perturbation. For brevity, the 'dew point' is not always mentioned in the naming. The temperature perturbations are constant with altitude, so no moist stabilization of the atmosphere occurs and the entire relative humidity profile is unchanged. The profiles of these scenarios are shown Figure 3.1 in In the naming system WARM and COLD mean a 4 Kelvin warmer and colder atmosphere respectively.

3.2. Model set up

The domain is a square of $192\mathrm{x}192km$ roughly representing the size Netherlands with a grid cell size of 200x200 m leading to 960x960 grid points in the horizontal. This is done vertically in 240 layers with an adaptive Arakawa C-grid. The grid is vertically spaced closer together near the surface $\approx O(40)m$ and the grid spacing increases linearly towards the top $\approx O(400)m$ in cross section 120 at 7 km altitude.

Radiative heating and cooling is prescribed and not computed interactively. It is assumed that radiative feedbacks are not dominant during the the time of the simulation. This assumption that radiative heating and cooling can be prescribed on a daily time scale may need reconsideration in further studies. It is
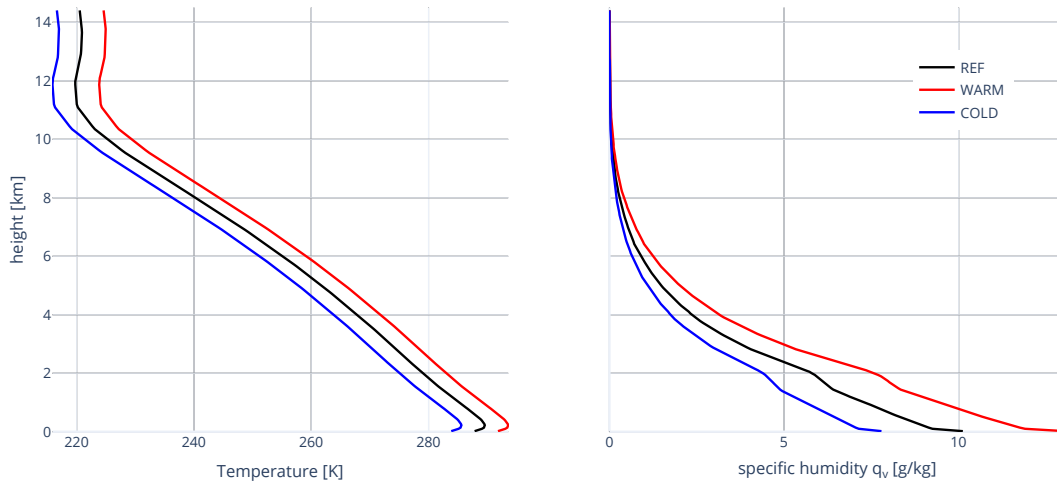
Figure 3.1: The input profiles of the reference scenario (REF), and the perturbed scenarios WARM and COLD

computationally costly to calculate these, therefore these feedbacks are neglected in this study.

The microphysics scheme utilizes a linear combination of cloud ice and cloud water as described in the appendix of Böing, Steven et al. (2012). This combination of ice and liquid water making up the clouds is termed 'condensed' water. The microphysics scheme is a single-moment scheme, more on what moment in this context means can be found in Molthan and Colle (2012).

The surface is represented without geography. This means both no topography, nor different land cover classes. The earth surface is a simple flat plate in the model. This idealization reduces heterogeneity in the surface forcing compared to reality. Heterogeneity is introduced artificially. The simulations are characterized by prescribed fluxes of heat and moisture from the surface, going through a diurnal cycle of 24 hours and then are kept at a minimum with 6 more hours of data available. This is shown in Figure 3.2 a). In addition, a forcing term due to large-scale convergence is supplied. This is associated with large-scale uplifting and shown in Figure 3.2 b). In other words, this term represents the passing of a synoptic scale low pressure disturbance. The low pressure destabilizes the atmosphere by providing moisture to the domain. This is represented in the model by increased moisture fluxes and increased cooling rates.
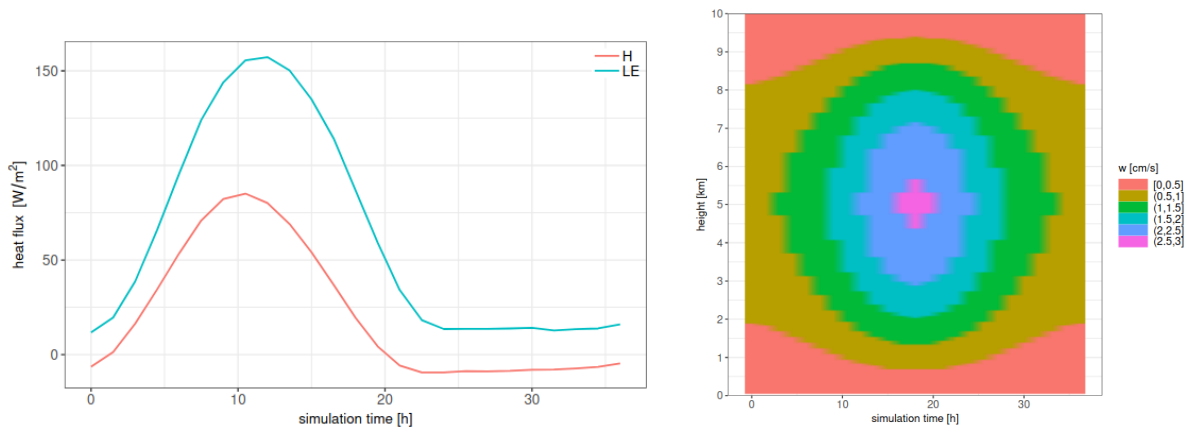
Figure 3.2: Figures S1 and S2 from Lochbihler et al. (2019). a) Surface forcings for the DALES simulations. Sensible (H) and latent heat (LE) fluxes. b) Idealized large scale forcing for vertical velocity w.

The boundaries at the sides are periodic to prevent energy leakage into or out of the model domain. The domain moves with the mean wind at 10 m/s to allow longer time steps in the computation. This has no effect on the dynamics of the atmosphere, and is a standard procedure of DALES. This translation

velocity keeps the storm motions (relative to the domain) low. A strong unidirectional wind shear is used, this is shown in Figure 3.3. In More specific information on how the mean wind profile is constructed can be found in Lochbihler et al., 2019.
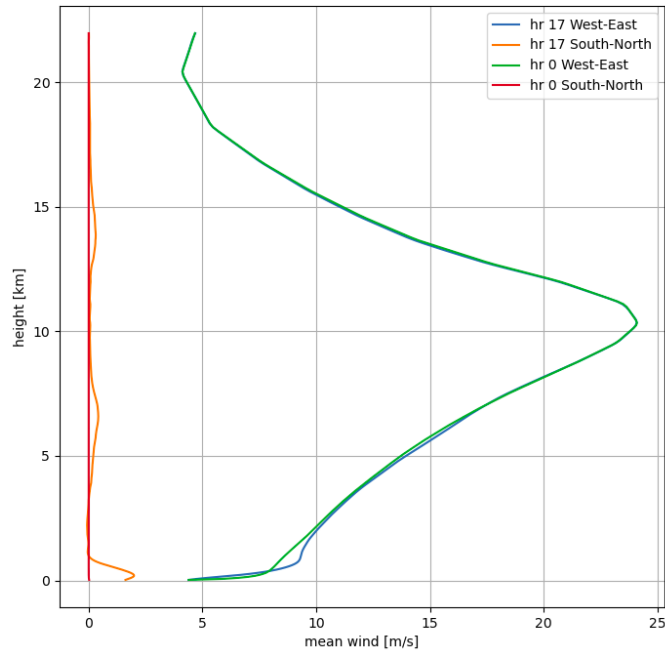
Figure 3.3: Vertical wind shear profile of the input mean wind profile in West-East direction, u, and in South-North direction, v. At initialization (hour 0) the input conditions are given and at simulation hour 17 the mean wind profile is shown.

3.3. Model outputs

3.3.1. Moisture variables

The moisture variables representing water in its various states are given as specific humidity. For water vapor this is q_v. For the water that makes up clouds, the sum of cloud ice and cloud water, this is the cloud condensed specific humidity, q_c. Together the water vapor and cloud condensed water make up the total specific humidity, q_t as defined in Equation 3.1.

Moisture is removed from the domain by the transformation of cloud condensed specific humidity into precipitation q_r. After it has formed, it starts to fall until it is removed from the domain at the Earths surface. The various specific humidity variables representing water in all its forms are illustrated in Figure 3.4.

Moisture is increased in the domain by the latent heat flux and by moisture flux due to large scale convergence. The moisture fluxes increasing q_t due to the large-scale convergence are not saved as outputs, complicating the reconstruction of a moisture budget.

$$q_t = q_v + q_c \tag{3.1}$$

3.3.2. Cross sections

In total 240 layers have outputs every minute for 30 hours. Of these layers, the layers in Table 3.1 have cross sections with outputs at each grid point. The other layers only have sampled statistics as outputs, these are described in Section 3.3.3.
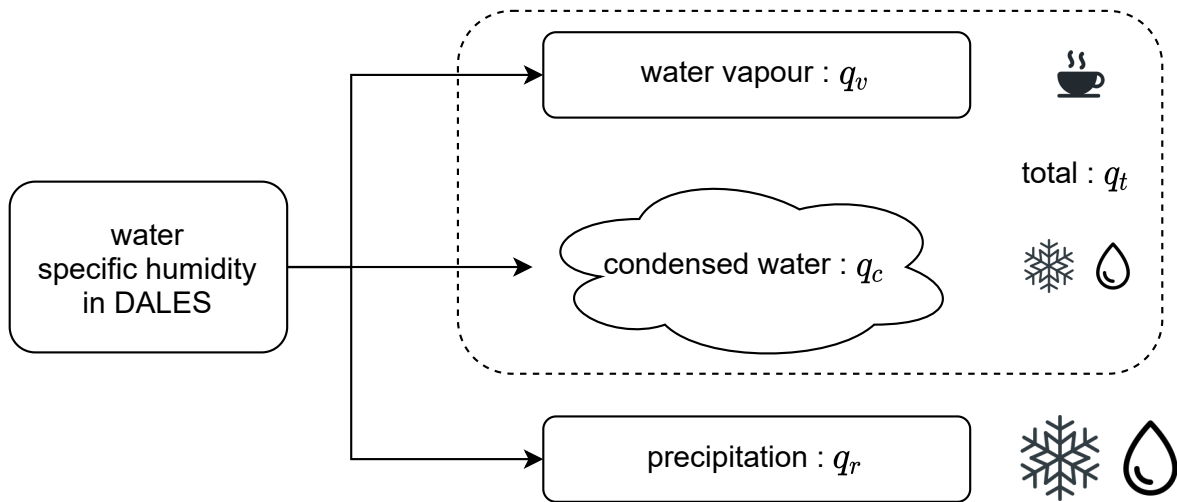
Figure 3.4: Flowchart showing the specific moisture variables that DALES uses. For intuitive understanding, the shape of liquid water droplets in the clouds and rain drops in precipitation are (mis)represented (Beard & Chuang, 1987). Water vapor is (mis)represented by steam visible above a tea cup. Whilst humans only see the liquid droplets, the depiction of visible steam is commonly associated with water vapor.

The grid is a staggered Arakawa C-grid with full levels and half levels. The half levels and full levels are both used throughout this report without explicitly mentioning which is used. Full levels are where horizontal velocities, u, v, are defined, whilst half levels are where the vertical velocities, w, are defined. The distance between the full and half-levels is assumed to be negligible for the calculation of fluxes. For notation, the half level values rounded to 1 decimal are used throughout this report.

level number	full level (zt)	half level (zm)	Appendix B classification
3	0.10	0.08	near surface ($\&$ sub-cloud)
13	0.52	0.50	sub-cloud
24	1.01	0.99	near cloud base
54	2.53	2.51	in-cloud
71	3.53	3.50	in-cloud
101	5.57	5.54	in-cloud
120	7.07	7.03	in-cloud

Table 3.1: heights of cross sections given in km, rounded to 2 decimal places

The cross-section heights can be classified as: near the surface, in the sub-cloud layer, near cloud-base, and within the cloud layer. Motivation for this classification can be found in Appendix B. The classifications are shown in Table 3.1 so the reader can follow what is meant when these classifiers are used in the text. These cross sections have the wind speeds u, v, w, the moisture variables from Section 3.3.1, the liquid potential temperature Θ_l and the virtual potential temperature perturbation Θ_v' available. The horizontal grid size of the model is 200m in both x and y directions. The simulations have in 50GB large datasets as outputs per horizontal cross section. Pressure fields were not saved for the cross sections, making it impossible to directly evaluate pressure perturbations.

3.3.3. Sampled statistics

Besides the direct model outputs, a set timeseries of statistics per cross section are available. Partly these are mean values, such as the mean pressure of a cross-section. For the other part these are conditionally sampled output statistics, that include the area fractions of the sampling. The conditional sampling is done according to the criteria in the DALES model sampling routine. Several logic tests can be applied (in combination) to define an updraft, they are constituted of condensed water presence, $q_c \geq 0$, positive buoyancy perturbation, $\Delta\Theta_v \geq 0$, and positive updraft velocity, $w \geq 0$.

<div style="text-align: right">

4

</div>

<div style="text-align: right">

Methods

</div>

This chapter presents a detailed description of the steps followed to produce the results of the work. This methodology follows the strategy outlined in Lenderink and Fowler (2017) to use models that explicitly resolve convection, such as the DALES model, to understand extreme precipitation.

4.1. Moisture transport

4.1.1. Moisture transport in updrafts

The amount of precipitation in the convective showers of interest is ultimately determined by the amount of moisture in the cloud that it's coming from. This water arrives in the cloud being carried skyward in updrafts. Reconstructing the condensed water in the cloud from the gradient of the saturation specific humidity as described in literature (e.g. Muller & Takayabu, 2020), see Section 2.1, is problematic. This is because the cross sections with data output as described in Chapter 3 are spaced too far apart to construct an accurate vertical profile of the lapse rate of condensation $\frac{\partial q_{sat}}{\partial z}$. Furthermore, testing showed that presuming constant equivalent potential temperature, one of the assumptions used in the derivation of Precipitation in Muller and Takayabu (2020) is questionable.

To solve the above problems, a different approach is used. The total specific humidity, q_t is used. q_t is a conserved quantity, with its flux representing the total moisture being transported. In Figure 4.1 it is illustrated what factors are determining for how much moisture is transported up into the cloud falls as precipitation P. Following the logic in the illustration an equation can be stated to calculate the moisture transport rate, F. This is done in Equation 4.1. This is under the assumption that the dominant mode of moisture transport is vertical advection.
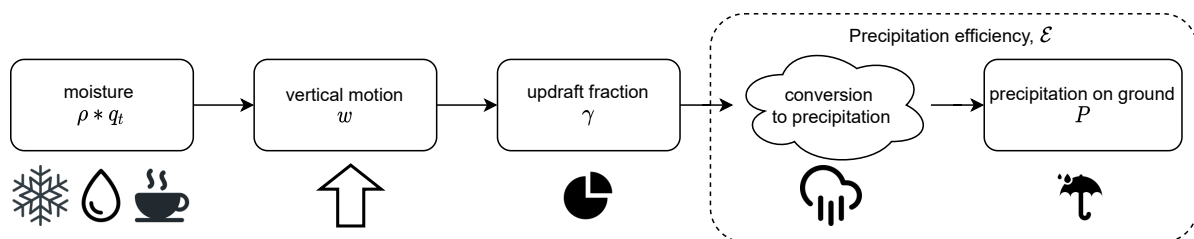
Figure 4.1: Flowchart of moisture transport in updrafts. For intuitive understanding, the shape of liquid rain drops in precipitation is (mis-)represented (Beard & Chuang, 1987). Water vapor is (mis-)represented by steam visible above a tea cup. Whilst humans only see the liquid droplets, it is commonly associated with water vapor.

$$F = wq_t\rho \tag{4.1}$$

Throughout the report, both the precipitation as the moisture transport are often reported in units of kg. Readers may be familiar with millimeters of rain instead. One millimeter of rain is the same as $1kg/m^2$

4.1.2. Moisture budget

Besides moisture transport in updrafts, more is at play. The amount of precipitation in the convective showers of interest is ultimately determined by the amount of precipitable water in the atmosphere. This water arrives in the cloud being carried skyward in updrafts and through the cloud entraining surrounding air through local convergence. In the entraining plume model in Section 2.2, the local convergence was the entrainment term. The total amount of water in the atmosphere is also influenced by losing moisture in downdrafts, whilst gaining moisture due to the large scale convergence. In the DALES runs this is implemented as having an additional moisture flux at altitude. The budget is illustrated in Figure 4.2.
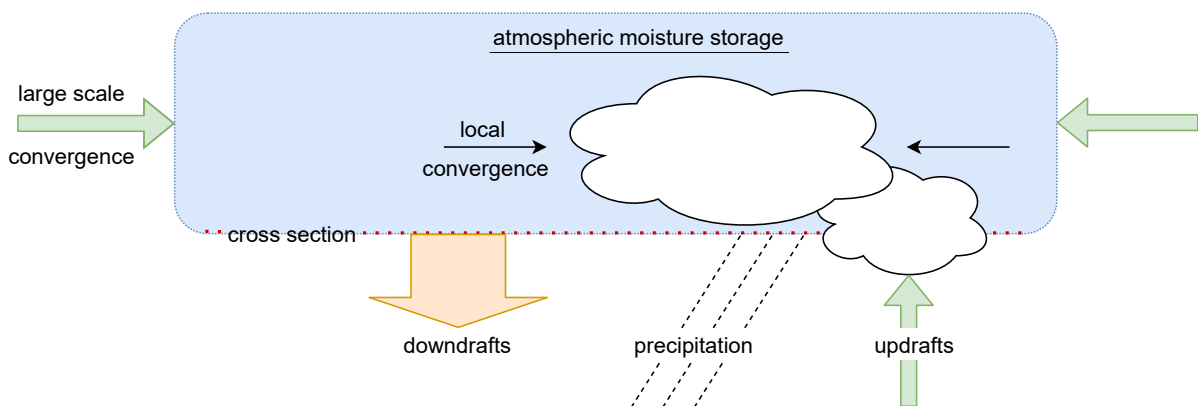
Figure 4.2: Illustration of the atmospheric moisture storage budget

The illustration in Figure 4.2 of the moisture in the clouds can be related to the large scale moisture budget, Equation 4.2. In this equation S is the storage term, named atmospheric moisture storage in Figure 4.2. M is the moist convergence, composed of the components with the all the wide arrows. E is the evaporation, providing moisture near the surface which eventually moves into the clouds in the updrafts in the convergence term.

$$S = M + E - P \tag{4.2}$$

As stated in Chapter 3, the large scale convergence fluxes are unavailable. Therefore, reconstructing the moisture budget is problematic and the scope of the problem is narrowed to the relation between the transport of moisture in updrafts and the precipitation.

4.2. The equation of vertical motion

From the Navies Stokes equations, the anelastic equation of motion can be derived. It can be written as Equation 4.3, similar to Houze (2014) Eq. 7.2

$$\frac{\partial \mathbf{v}}{\partial t} = -\frac{1}{\rho_0}\nabla p' + B\mathbf{k} - \mathbf{v}\cdot\nabla\mathbf{v} \tag{4.3}$$

To focus at the vertical component, the advection term $\mathbf{v}\cdot\nabla\mathbf{v}$ is simplified to .

$$\mathbf{v}\cdot\nabla\mathbf{v} = w\frac{\partial w}{\partial z} + v\frac{\partial w}{\partial y} + u\frac{\partial w}{\partial x} \tag{4.4}$$

The last two terms are related to horizontal advection, which is mainly a movement with the horizontal flow. The horizontal advection terms are neglected. This leaves four terms with not enough information to reconstruct the entire equation. It is possible however to determine the what causes more acceleration, horizontal convergence or local buoyancy.

- Buoyancy B which is output in DALES as Θ'_v
- Vertical advection $w\frac{\partial w}{\partial z}$. This term can estimated from by taking the continuity equation, replacing $\partial w/\partial z$ with the horizontal convergence, $-\partial u/\partial x - \partial v/\partial y$
- Pressure perturbations $\frac{1}{\rho_0}\nabla p'$, which are unknown
- Change of velocity in time $\partial \mathbf{V}/\partial t$

4.2.1. Buoyancy

Positive buoyancy is expected to drive parcels up. Intuitively one may relate this to 'warm air rises'. Buoyancy is defined as acceleration in Equation 4.3, but it can be retrieved from the perturbation of virtual potential temperature Θ'_v using Equation 4.5 by multiplying with the gravity acceleration, g, and dividing by the reference $\Theta_{v,0}$ which combined is approximated as a division of a thirtieth $\frac{9.81}{\sim 300} \approx 30$. Even if this constant is slightly off, the conversion is done consistent for all buoyant acceleration and therefore the exact value is less relevant when comparing scenarios.

$$B = \frac{g}{\Theta_{v,0}}\Theta'_v \tag{4.5}$$

4.3. Selecting relevant updrafts

To investigate where the moisture transportation leads up to intense precipitation, a mask is generated on the horizontal cross sections. A set of conditions is used to determine what a cloud is. Clouds can be made of liquid water or ice or both. These states of water are contained in the cloud condensed specific humidity q_c. So threshold values were tested for the variable, q_c. After testing, the threshold value of $q_c > 0.1$ g/kg is selected to define cloudy areas.

The isolines containing the threshold value of cloud condensed water are shown in Figure 4.3. Other masks are also shown for updrafts and cloud cores. The cloud core is defined here as being buoyant, within the cloud and having at least a small upward speed.
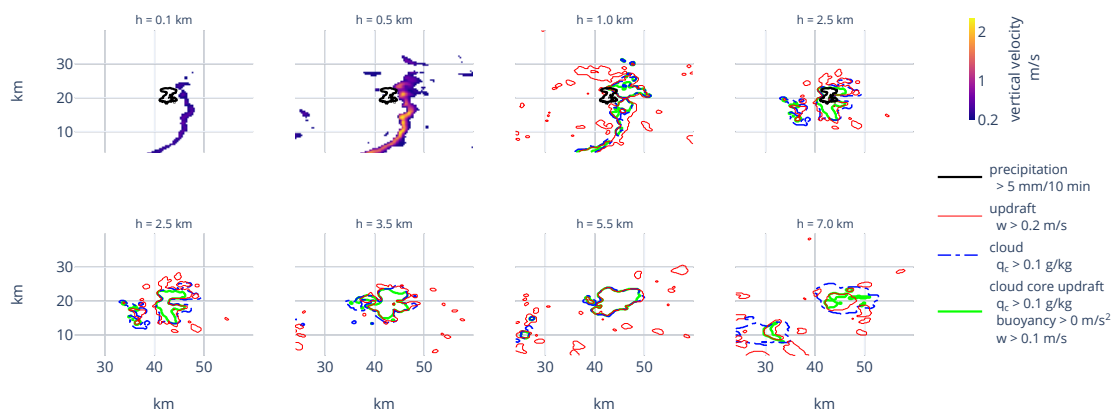
Figure 4.3: Snapshot at the start of phase-II of the reference scenario. Only part of the domain is shown. Visible are the conditional masks used to identify where the moisture transport is happening. The sub-cloud layers have vertical velocities w > 0.2 m/s, whilst the higher layers have different masks shown as contour outlines. The top row panels also include a surface precipitation outline in black where the surface precipitation rate > 5 mm/10 minutes is shown.

4.4. Yield and rate

Similar to how Lochbihler et al. (2019) define precipitation yield and precipitation rate, here yield and rate are distinguished. Not only for precipitation, but also for moisture transport (moisture fluxes). The explanation is easiest with surface precipitation, but the same holds for other quantities such as moisture transport. These concepts can more easily be understood with the illustration in Figure 4.4.

Yield is the sum of a quantity being transported trough a cross section divided by the number of grid points in that cross section. This gives a mean value for the entire domain. Taking the sum of the precipitation rates P_r of the cells with precipitation and dividing this by the domain area this gives the domain yield: $P_{yield} = \frac{\Sigma P_r}{A_D}$

Rate is the sum of a quantity being transported through the points that have more precipitation or transportation than the set threshold. This gives a mean value for the participating points. If for example thresholds on q_c (e.g. $q_c > 0.1 g/kg$) are used to define transport in the clouds only, the mean rate of the domain gives the average of transport in the cloudy grid cells. This domain mean rate is found by summing the precipitation rates and dividing by the area of the precipitating cells: $P_{rate} = \frac{\Sigma P_r}{A_P}$
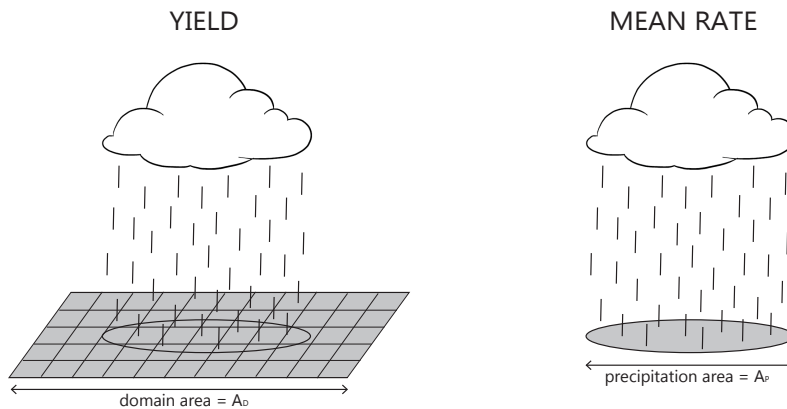
Figure 4.4: Illustration of yield and rate for surface precipitation. The domain yield is found by summing the rates and dividing over the area of the entire domain. The domain mean rate is found by summing the rates in a cross section and dividing over the area where precipitation hits the surface.

4.5. Period of interest

To investigate the processes of interest with reduced computational cost, some analyses are done only for the time of interest. The motivation for how this time span is determined is given here.

Convection needs time to organize and since precipitation is of interest, this gives a qualitative indication of a miminum time of interest. Besides a minimum, there is also a maximum to the time of interest. Towards the end of the simulations, surface fluxes are minimal and influence of the initial condition decreases. This implies that the large-scale lifting, being identical in all simulations, becomes more dominant and leads to a convergence of the output parameters to similar values. Therefore the latter hours of the simulations are not analyzed in detail.

Lochbihler et al. (2019) characterized two active precipitation phases, with the same time span for all simulations. This temporal evolution can be summarized as follows: After the onset of precipitation at hour 11, an initial phase-I of unorganized convection with active precipitation occurs. This is followed by a period of recovery. During the recovery, the moisture lost in phase-I is replenished by the fluxes into the domain. After the recovery period, a second active phase of precipitation is defined for the 3 hours surrounding simulation hour 17. This phase-II has organised convection with the highest precipitation

rates.

For this research, the analysis in Lochbihler et al. (2019) is followed and the phase-II is used as the period of interest.

4.6. Pre-processing

In the presented work, pre-processing is done. Here we present why and when filters are applied. Numerical noise was present in the data, which could be due to the second order advection scheme in DALES.

The types of filters applied can be categorized as spatial and temporal. An overview is given in Figure 4.5. The pre-processing steps will be treated separately in 4.6.2 and 4.6.1.
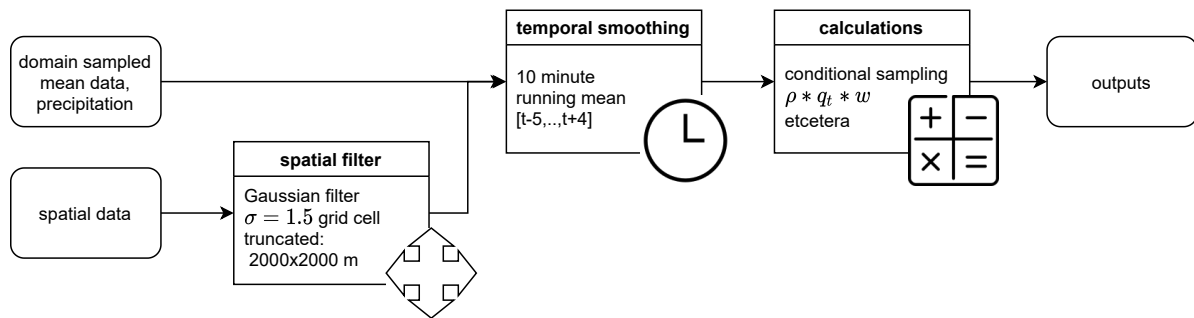
Figure 4.5: Flowchart of the filters applied on the raw DALES model outputs leading to output data ready for further processing and visualization.

4.6.1. Spatial filtering

Whenever used, the spatial filter is to make segmentation algorithms perform better and remove numerical noise from the outputs. This spatial filter is a gaussian filter which in practice smears values out over a a block of 2000x2000m with a peak value in the centre as shown in Figure 4.6.
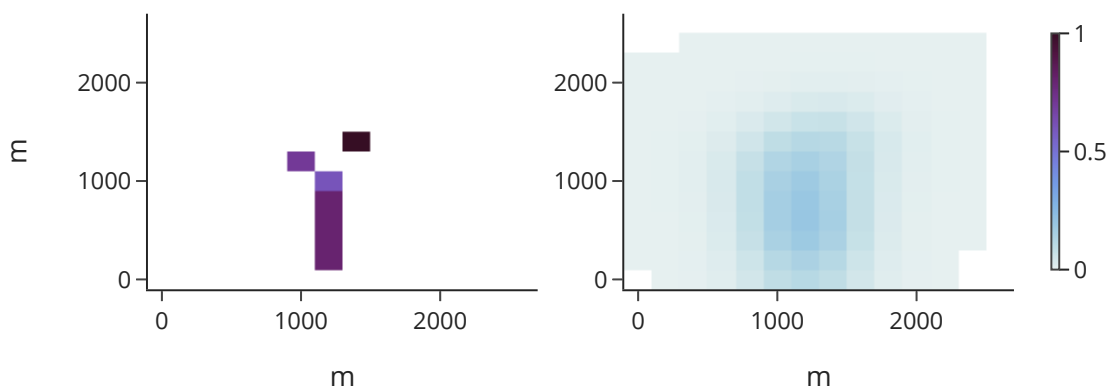
Figure 4.6: Region of influence of 10x10 grid cells of the spatial gaussian filter used for an arbitrary pattern

4.6.2. Temporal smoothing

Since urban drainage design is not done with instantaneous per second rainfall, the data is aggregated to 10 minute values. This is the same as filtering by smoothing instantaneous values. The data is aggregated to mean values with a 10 minute long block filter and this is done after calculations are made as a final post-processing step to make plots visually more palatable. To reduce phase delays being introduced by the temporal filter, it is centered around the timestep with 4 minutes 'into the future', the timestep itself and 5 minutes 'in the past'. The effect of this filter is compared to instantaneous quantities without filtering and hourly quantities in Figure 4.7. In the instantaneous data a lot of noise is present, whilst in the hourly it is very smoothed out and secondary structures become similarly strong as the primary gust front.
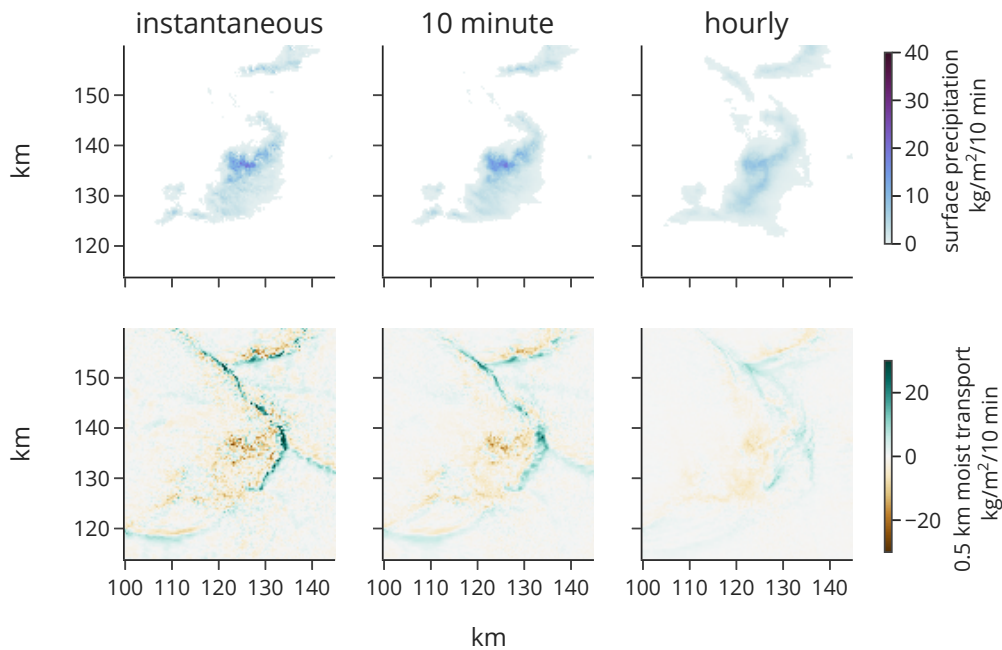
Figure 4.7: Different temporal smoothings on a snapshot at simulation hour 17, with Precipitation in the top row smaller than 0.1 mm/10min masked as in Lochbihler et al., 2019. In the bottom row, the moisture transported vertically at 0.5 km altitude is shown. To make values comparable, the instantaneous values are multiplied by 10 minutes, whilst the hourly values are divided by 6.

4.7. Post-processing

To make the 1 Terabyte of unfiltered data and the 500 GB of filtered data more manageable within the limited computational memory and power, various post-processing steps were taken. The data was reduced by only taking outputs of the filtered data at every 10th minute.

A separate sub-Section is dedicated to how climate scaling coefficients are calculated with Section 4.7.1

Independence of the data is guaranteed by sampling only independent points. The technical details of this are described in Section 4.7.2. For binning procedures, spatial independence of sampled data is not required. Subsampling is not done for binning procedures from a data-independence point of view.

4.7.1. Climate scaling coefficients of variables

climate scaling The climate scaling can be found per degree Kelving using the geometric mean. This is expressed as a percentage of growth per degree of warming in Equation 4.6. From a variable, for

example x here, a relative climate scaling can be determined from the perturbed simulations. This is done by taking the difference Δx of the variable between two simulations. The definition is used that climate scaling is positive with warming if that variable increases at an exponential rate. Equation 4.6 can be simplified to two applications of the Equation in which the arbitrary variable w can be replaced with any variable. These two applications are given in Equations 4.7 and 4.8.

$$1 + \alpha_x = (\frac{x_{REF} + \Delta x}{x_{REF}})^{1/\Delta T} * 100\% \tag{4.6}$$

$$\alpha_{x,WARM} = ((\frac{x_{WARM}}{x_{REF}})^{1/4} - 1) * 100\% \tag{4.7}$$

$$\alpha_{x,COLD} = (1 - (\frac{x_{COLD}}{x_{REF}})^{1/4}) * 100\% \tag{4.8}$$

4.7.2. Subsampling for correlations

After pre-processing is done, subsampling may be necessary. For correlations calculated from the data, the filters introduce a dependence on the neighboring points. For the spatial filter, the dependent points are the block of 10x10 nearest neighbors. For the temporal filter these are the 10 minutes as previously shown in Figure 4.5. Thus calculated correlations from this neighboring zone of influence would be artificially high because samples are not independent. Besides that, taking a reduced amount of points is beneficial in reducing computational cost. Therefore correlations are determined by subsampling every 10th point in x and y direction every 10th minute. For the 3 hours of interest this leaves enough data points (165888 points) to calculate with for robust statistics.

For the calculation of percentiles in the period of interest, subsampling was applied in the time dimension only. Every 10th minute all data points in a cross section are taken. There is no spatial subsampling. These timesteps are then grouped together and the percentile for this entire phase-II is calculated. Wherever other approaches are used for subsampling, they are explicitly mentioned.

For visual representation, plotting many data points leads to overplotting. This can be understood by the freely translated Dutch folk proverb "Not seeing the forest between the many trees". To prevent this overplotting, various subsampling strategies are applied, always taking the minimal spacing used for the correlation calculations. Figures that do show correlations or percentiles together with a scatter of datapoints thus have more points used for the correlation coefficients than the amount visually depicted in the figure.

5

Results

This Chapter presents a selection of results aimed at providing direct or indirect evidence and quantification of the consequences of a warming climate. Differences between the simulations are highlighted. Focus is put on comparing the Climate scenario with 4 Kelvin cooling compared to REF of the initial vertical atmospheric profile (COLD) and WARM simulations, since differences are easiest to present. For brevity, the REF result is not always shown, but the results for REF are somewhere in the middle of the other results.

This Chapter starts with showing how convection grows deeper and more vigorous in the cloudy layer in Section 5.1. This mainly provides insight into how updrafts in cloudy layers change with warming, yet the sub-cloud layer is not forgotten.

After that, cold-pools dynamics are discussed in Section 5.2. There, it is first shown how cold-pool structures grow in size with warming and how they increase convergence and buoyancy perturbations. Finally the importance of convergence over buoyancy for the generation of updrafts is shown. The convergence however, is not important anymore higher in the clouds. This is shown in Section 5.3.

A more three dimensional picture is then needed to connect what is happening in the cross sections. This is done in Section 5.4 by first putting snapshots of normalized velocities next to each other. After that statistical analysis is done on the connections by linking positions in one layer to one above it.

With knowledge of how the dynamics change, it is subsequently time to get to the heart of the matter, moisture. More specifically into where moisture is transported through cross sections. What warming does to the probability distribution tail of moisture transport. And finally how the recipe for moisture transport can be dissected into ingredients.

5.1. Updrafts in cloudy layers

In a warmer scenario, updrafts in the clouds become more vigorous. This section first presents how the time response on average is in Section 5.1.1. After this, a zoom in to strong updrafts is made in Section 5.1.2. Subsequently, the found precipitation yield climate scaling during the organized phase is found in Section 5.1.3. The sweet spot at which to select the strong updrafts in Section 5.1.2 is considered in Section 5.1.4. Using this sweet spot, the scaling coefficients of strong updrafts are presented in Section 5.1.5. Finally, a view along the entire height of the relevant atmospheric column is taken. The vertical profiles of updraft speed- and subsiding speed scaling are provided in Section 5.1.6.

5.1.1. Cloudy updrafts

Cloudy parcels of air become more buoyant due to increased buoyancy production from latent heat release. More water vapor q_v is converted to cloud condensed water q_c. This releases more heat in the cloudy updrafts. The extra heat release makes the buoyant acceleration greater. To give a feel of how the updrafts change within cloudy grid cells, the cloudy updrafts are shown in Figure 5.1. From the cold to the warm scenario, the onset of deep convection is slightly later. After the onset of higher vertical in the cloud updrafts, the resulting convection is deeper.
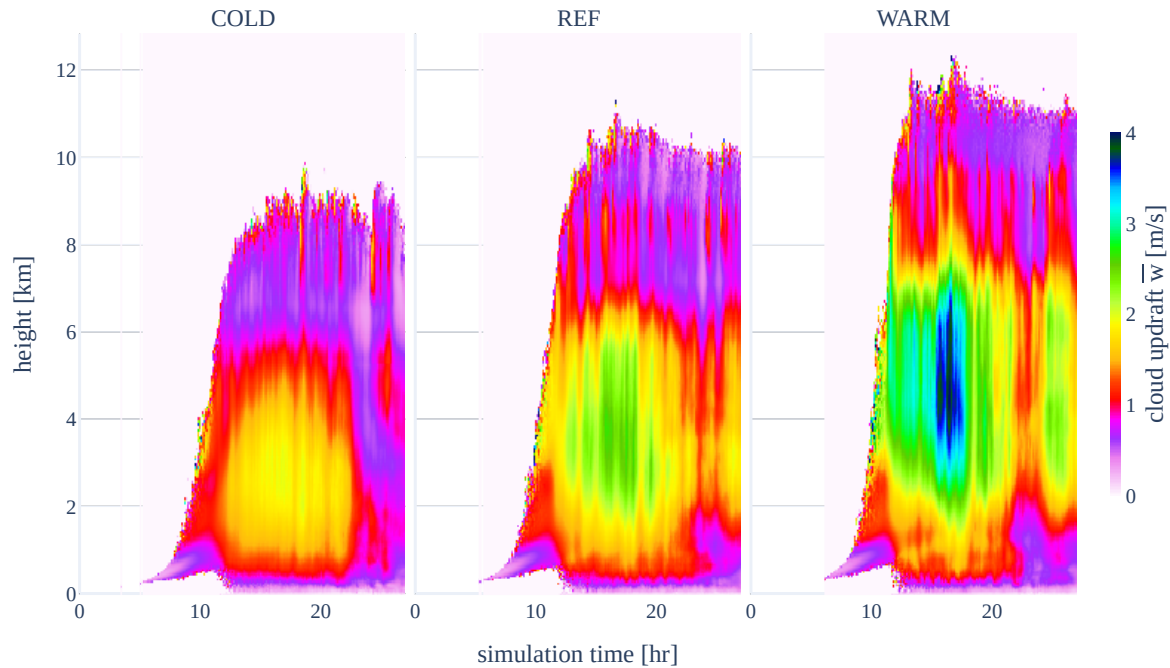
Figure 5.1: The slab averaged cloudy updraft velocities for $q_c > 0$ and $w > 0$. The left panel shows the 4 Kelvin colder simulation Climate scenario with 4 Kelvin cooling compared to REF of the initial vertical atmospheric profile (COLD), the middle the reference simulation REF and the right panel shows the 4 Kelvin warmer simulation WARM.

5.1.2. Climate scaling of strong updrafts in the clouds

Strong updrafts become increasingly stronger for the warmer simulations. The order of the updraft absolute response logically follows the starting temperature of the simulation. The increase in strength with warming, is in other words that climate scaling is positive. The magnitude of the climate scaling depends on what threshold for strong is used and which height is observed.

Stronger updrafts are selected by taking higher percentiles of vertical wind speed. The climate scaling of the strong updrafts at the 99.5th percentile are shown in Figure 5.2 as α_w.

The strength of strong updrafts in the clouds is related to the production of convective precipitation. Strong updrafts show a temporal correlation to domain precipitation yield. This temporal shape similarity can be seen in Figure 5.2, by comparing the surface precipitation yield with the 99th percentile of updrafts per simulation. The coefficients of determination, r^2 of the timeseries are shown in the legend at the precipitation entries.

Lochbihler et al. (2019) define two phases of precipitation in the simulation outputs. One phase with 'popcorn' convection, a period of less activity and a second phase called the organized phase. This two phased response is also found in the updraft speeds. The response is found the higher percentile updrafts in the cross sections containing clouds. In Figure 5.2, the two phases of precipitation response are clearly visible for the WARM and REF simulations, but not for the COLD simulation. The COLD simulation has less organisation into cold-pool structures, which may dampen the peaks in the

precipitation intensity response. The organized phase period is marked with the grey box.
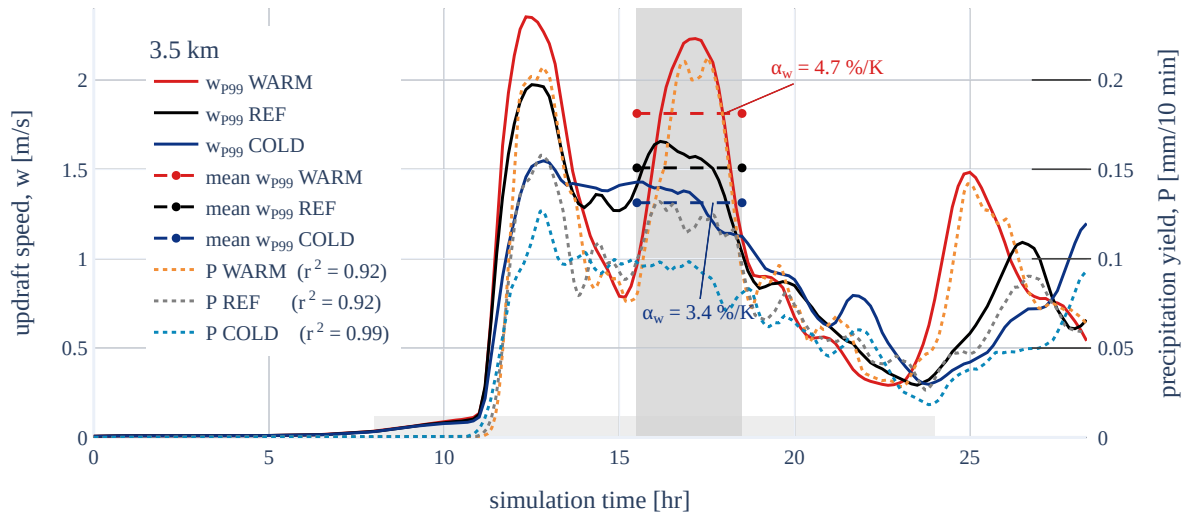
Figure 5.2: Strong updrafts selected with the 99th percentile of vertical speeds in a cross section at 3.5 km. The organized phase is marked in dark grey. Climate scaling coefficients α_w are determined with respect to the organized phase mean values. Coefficients of determination r^2 are determined on the timeperiod marked in light grey near the vertical axis origin.

5.1.3. Scaling coefficients of precipitation yield

Compared to the reference simulation, precipitation yield in the WARM simulation has a climate scaling that exceeds the CC scaling rate. The climate scaling of the COLD scenario precipitation yield does not exceed CC scaling. The climate scaling rates are shown in Table 5.1.

Table 5.1: Climate scaling of the mean precipitation yield in the organized phase. Climate scaling is determined based on the 180 minutes of 10 minute precipitation output in the organized phase

Precipitation yield	α_{COLD}	6.7 %/K
	α_{WARM}	8.5 %/K

5.1.4. Temporal relation as a sweet spot selector

Climate scaling of updrafts at a percentile is sensitive to the choice of height and percentile. In this section the choice for the combination in is motivated. The shape similarity of the 10 minute updraft speed and the precipitation output is used as the determining metric.

Temporal relation to select the most representative percentile-height combination

Climate scaling coefficients and the linear correlations with precipitation are sensitive to the chosen percentile and the height of the cross section. To select updrafts best related to precipitation yield, the temporal coefficients of determination r^2 are determined for many scenarios. The r^2 coefficients give a quality indication of linear relationships. From the available scenario combinations of percentile and height, the best set is chosen subjectively from Table 5.2. The chosen scenario is outlined in red and was used for Figure 5.2. Some more timeseries of the updraft response in the vicinity of the sweet spot can be found in Appendix A.1.

Table 5.2: The temporal coefficients of determination, r^2, of the linear relations between the updrafts and surface precipitation yield. The updrafts are taken at the 90th, 95th, 98th, 99th, 99.5th, 99.9 and 99.99th percentile of the velocity distributions respectively. These coefficients percentiles are found from 6 timesteps per hour in overlapping hourly bins. A total of 5529600 points are used for percentile determination. Temporal correlation is determined over simulation hours 8-24 with 96 timesteps of 10 minutes.

	P90	P95	P98	P99	P99.5	P99.9	P99.99
7.0 km height							
7.0 COLD	0.63	0.68	0.76	0.79	0.78	0.66	0.36
7.0 REF	0.53	0.62	0.77	0.74	0.66	0.6	0.59
7.0 WARM	0.32	0.61	0.95	0.95	0.91	0.77	0.65
5.5 km height							
5.5 COLD	0.64	0.65	0.64	0.59	0.54	0.5	0.63
5.5 REF	0.48	0.71	0.93	0.92	0.88	0.78	0.7
5.5 WARM	0.4	0.77	0.94	0.97	0.93	0.76	0.63
3.5 km height							
3.5 COLD	0.53	0.76	0.79	0.92	0.91	0.73	0.59
3.5 REF	0.58	0.76	0.76	0.92	0.93	0.78	0.68
3.5 WARM	0.64	0.87	0.9	0.99	0.95	0.79	0.65
2.5 km height							
2.5 COLD	0.72	0.51	0.73	0.91	0.93	0.79	0.65
2.5 REF	0.72	0.61	0.72	0.88	0.9	0.77	0.67
2.5 WARM	0.65	0.76	0.84	0.91	0.9	0.72	0.56
1.0 km height							
1.0 COLD	0.29	0.39	0.67	0.84	0.92	0.86	0.69
1.0 REF	0.45	0.48	0.7	0.84	0.9	0.88	0.76
1.0 WARM	0.59	0.61	0.76	0.89	0.93	0.86	0.7
0.5 km height							
0.5 COLD	0.21	0.41	0.64	0.8	0.88	0.91	0.79
0.5 REF	0.28	0.46	0.7	0.81	0.88	0.87	0.77
0.5 WARM	0.38	0.53	0.75	0.85	0.87	0.81	0.72
0.1 km height							
0.1 COLD	0.3	0.49	0.69	0.81	0.89	0.9	0.79
0.1 REF	0.34	0.52	0.72	0.82	0.88	0.85	0.76
0.1 WARM	0.39	0.55	0.72	0.8	0.83	0.77	0.67

Where the sweet spot is

A few observations can be made about Table 5.2. The color shading with blue numbers having a higher value help paint the bigger picture. The values of r^2 have a 'sweet spot'. Temporal correlations between strong updrafts and precipitation yield are high here, consequently so is r^2. These higher values are present around the 99th percentile. The lower cloud layers at 2.5-3.5 km limit the vertical extent of this sweet spot. Note that this sweet spot behaviour is dependent on the size of the data used to determine the percentiles.

The description here is applicable only to the data when filtered, subsampled per 10 minutes and binned into overlapping hourly bins. No shifting in time is applied. The general concept that there is a region of combinations of percentile and height which has the best linear relation to the precipitation output does still hold.

Higher than the sweet spot

In the higher cloud layers 5.5 and 7 km, r^2 is lower for the colder simulations. The strong updrafts do not penetrate as deep in the cold scenario, therefore the temporal response is less present in these higher layers. Precipitation formation is likely to be less higher up for the colder simulation as well, this decreases the physical relationship between the surface precipitation and the updrafts here.

Testing showed that in general, climate scaling coefficients increased for the higher cloud layers.

Below the sweet spot

Weaker updrafts might not reach the clouds. Below the sweet spot, the near cloud base and sub-cloud updrafts still have good linear relations to the precipitation yield. In the 90th and 95th percentiles, lower numbers can be seen for the weaker updrafts though.

5.1.5. Scaling coefficients of updraft strength

The 'sweet spot' in the previous Section gives a basis to narrow down which updrafts relate to precipitation yield production. The climate scaling coefficients α are determined for the COLD and WARM simulations with respect to the REF simulation.

For every degree of degree of warming, updraft strengths increase. And vice versa, for every degree of cooling updrafts weaken. Higher up in the clouds the increase in updraft strength is higher. In the WARM simulation, updrafts do not necessarily strengthen in near the surface. The result is shown in Table 5.3.

Table 5.3: Climate scaling coefficients α of the strong updrafts of the 99th and 99.5th percentile. The COLD α are displayed with a negative sign to give an intuitive color scaling to the data.

	$-\alpha_{w,COLD}$ [%/K] @ P99	$-\alpha_{w,COLD}$ [%/K] @ P99.5		$\alpha_{w,WARM}$ [%/K] @ P99	$\alpha_{w,WARM}$ [%/K] @ P99.5
7.0 km	-15.0	-22.5		20.7	16.5
5.5 km	-13.9	-13.2		10.0	08.5
3.5 km	-3.4	-4.6		4.7	4.7
2.5 km	-1.6	-2.5		3.7	3.4
1.0 km	-1.9	-2.8		2.1	2.2
0.5 km	-3.7	-3.7		1.3	1.9
0.1 km	-2.9	-3.0		-0.1	0.4

5.1.6. Vertical profiles of strong speed scaling

Strong updraft scaling

Strong updrafts have stronger climate scaling higher up in the clouds. In the left panel of Figure 5.3, it can be seen that the absolute velocities have become increasingly different between the simulations higher up in the clouds. This is reflected in the high scaling coefficient α_w in the upper layers of the right panel.

Similar tests were also done with bins that only spanned one simulation hour instead of the entire organized phase. These tests revealed that, at lower percentiles in the lower layers negative relative scaling of updrafts incidentally occurs. The statistics were made more robust by filtering and taking all three hours of the organized phase. With the improved data, the negative climate scaling behaviour did not occur any more. With the filtering procedure the sensitivity of the results to the percentile chosen was reduced. The updraft strength selected with the 95th, 99th, 99.9th and 99.99th percentiles all qualitatively similar behaviour. Positive scaling behaviour is the rule for updrafts selected. The only exception is the 95th percentile near the surface with a small negative scaling coefficient of -0.1 %/K. The percentiles not displayed here can be found in Appendix A.2.
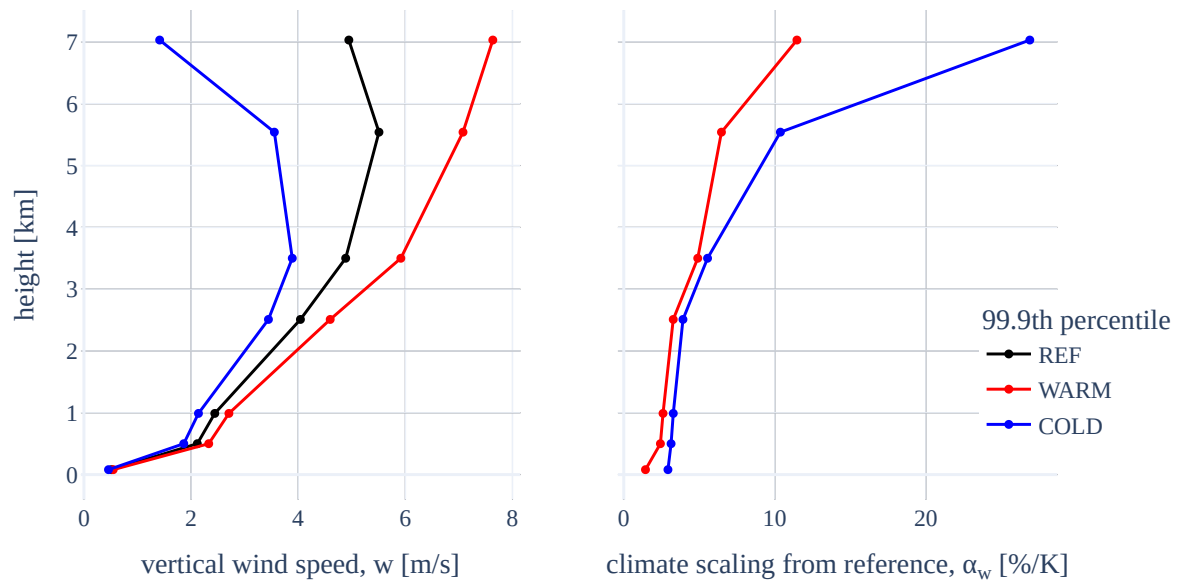
Figure 5.3: Updrafts in a height profile. Vertical profiles of absolute values and relative scaling of updrafts. These updrafts are the 99.9th percentile of the filtered wind speeds sampled every 10 minutes in the organized phase.

Subsiding speed scaling

Besides updrafts, downward motions are also part of the dynamics. Subsiding air has the highest speeds in the sub-cloud layer. With a warmer simulation, vertical movements of air masses strengthen. Subsequently, subsiding air has a positive climate scaling in magnitude. That is, the vertical motion velocities become more negative. Downdraft motions are invigorated by increased evaporation of precipitation.

The subsiding motions and their climate scaling at the 2nd percentile of all vertical motions is visible in Figure 5.4. Here, the second percentile is used to select the larger areas of descending air as seen in Figure 5.5. The subsiding air in the sub-cloud layer does indeed subside faster. Furthermore the downward motions are invigorated in the entire column except for COLD in the highest cross section. In the higher layer of the COLD simulation, the less deep convection compared to the REF simulation. If convection is not pushing air up, also no air is forced to subside by mass continuity.

The result shown here is not sensitive to the choice of percentile for the selection of subsiding motions. Taking the 0.05th, 0.1th, 1st and the 3rd percentiles gives qualitatively similar results. The difference between the percentiles is just the subsidence speed. At the lower percentiles, stronger downward motions are selected. A selection of percentiles used for sensitivity analysis can be found in Appendix A.2.
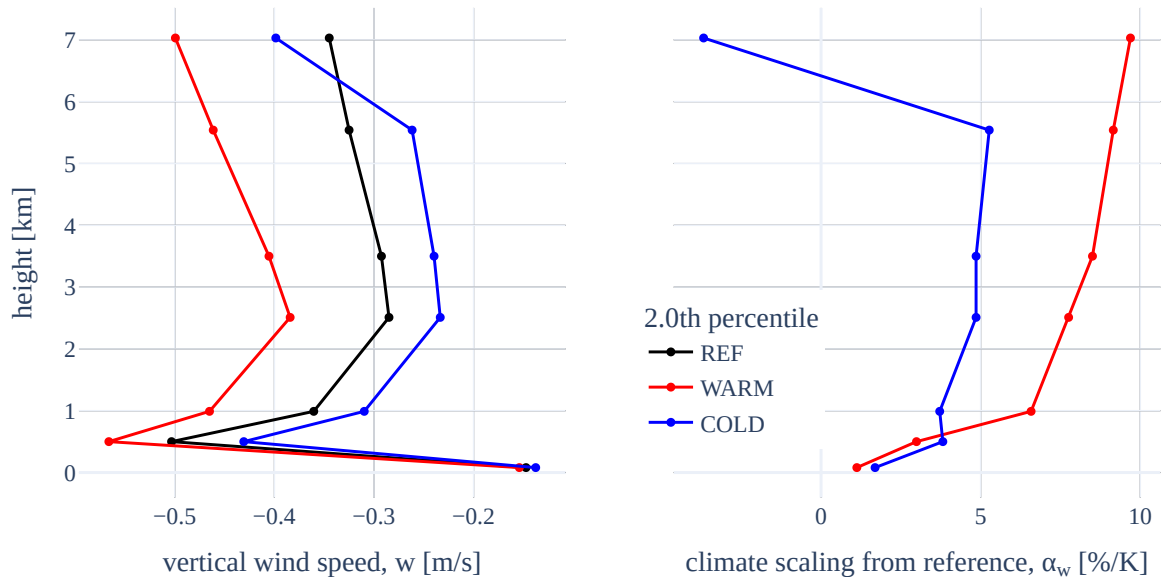
Figure 5.4: Vertical profiles of absolute and relative scaling of downdrafts. These downdrafts are the 2nd percentile of the filtered wind speeds sampled every 10 minutes in the organized phase.

Subsiding motions cover a larger portion of the domain than updrafts and have lower vertical motion velocities. In all simulations, testing with the 50th percentile showed that all 7 cross sections had small negative velocities throughout the simulation. This is an indirect hint to the updrafts being concentrated in small areas with large areas of slowly descending air.

5.2. Cold pool strength

For a warmer simulation, cold-pools become bigger and their buoyancy perturbation increases. This changes horizontal wind speeds such that at the outflow boundaries convergence increases. Consequently, stronger updrafts are organized into bigger gust fronts structures. In Section 5.2.1, the increasing size of updraft gust front structures is shown. In Section 5.2.2, the implication of the stronger cold-pools on buoyancy and convergence is presented. In Section 5.2.3 the importance of buoyancy and convergence for vertical motions near the surface is compared.

5.2.1. Increasing size of gust front structures

Cold-pools dynamics are driven near the surface by downdrafts. As the air travelling down reaches the surface, it spreads out into the so-called cold-pools. These then spread out near the surface, with a gust front near the outflow boundary. With warming, the downdrafts spread into spatially bigger cold-pool structures.

The spatially bigger cold-pool structures have invigorated near surface gust fronts. In Figure 5.5, the gust front structures of the COLD and WARM simulations are compared.

This figure combines updrafts in the nea-surface layer with the regions of downdrafts and the intensely precipitating areas in a snapshot of the entire domain. It can be seen that less, but longer gust front lines are present in the warm scenario compared to the cold scenario. And more grid cells exceed the higher threshold of 0.5 m/s updraft velocity in the warm scenario. The cold-pools are not round as often seen in tropical simulations, but the precipitating core is off centered due to wind shear. This agrees with the work of Lochbihler et al. (2019), Lochbihler et al. (2021) and Haerter and Schlemmer (2018).
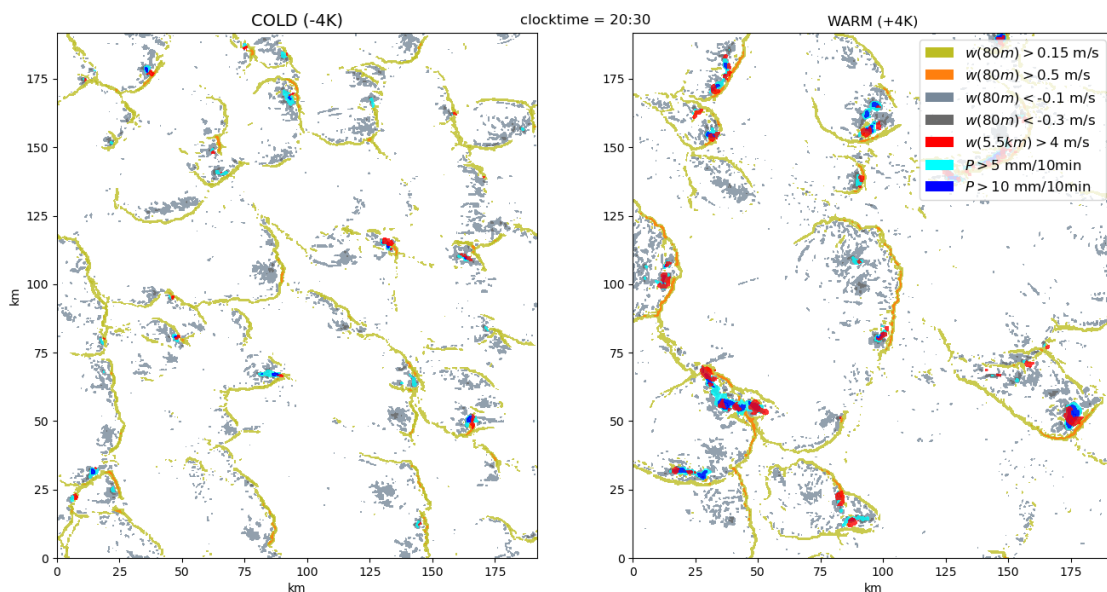
Figure 5.5: Spatial snapshot at simulation hour 16:30 showing near surface gustfronts, precipitation and strong cloud updrafts for the perturbed scenarios. The gaussian spatial filter has been applied, but the vertical velocities are instantaneous. The gustfront updrafts are visible in olive/orange and the in-cloud updrafts in red. The colors match the colors of the concepts in the feedback loop in Figure 2.6. This figure was part of a scientific presentation and is reproduced with authorization (Bentvelsen et al., 2021)

5.2.2. Convergence near the surface

From the equation of vertical motion (Equation 4.3) it can be understood what drives updrafts. Horizontal convergence, buoyancy and pressure perturbations can cause updrafts and downdrafts depending on their sign. Negative convergence is called divergence.

Due to the outputs lacking pressure perturbations, a force equilibrium can not be made. However, the equation of vertical motion can not be solved. The contributions of buoyant acceleration and horizontal convergence can be compared.

The cold-pool dynamics near the surface increase horizontal convergence at the gust fronts. Horizontal divergence increases where the downdrafts descend onto the near surface layer. The cold-pools have a negative buoyancy perturbations within their boundary. In the WARM simulation, the buoyancy perturbation is stronger. The cold-pools strength has a positive climate scaling. In Figure 5.6, the colder simulation in the top row can be compared with the invigorated values for all three variables in the warmer simulation in the bottom row. Here the increasing size of cold-pools with warming can be seen. The downdrafts are located in the areas of negative buoyancy, whilst the updrafts reside where buoyancy is neutral, the buoyant acceleration is zero here.
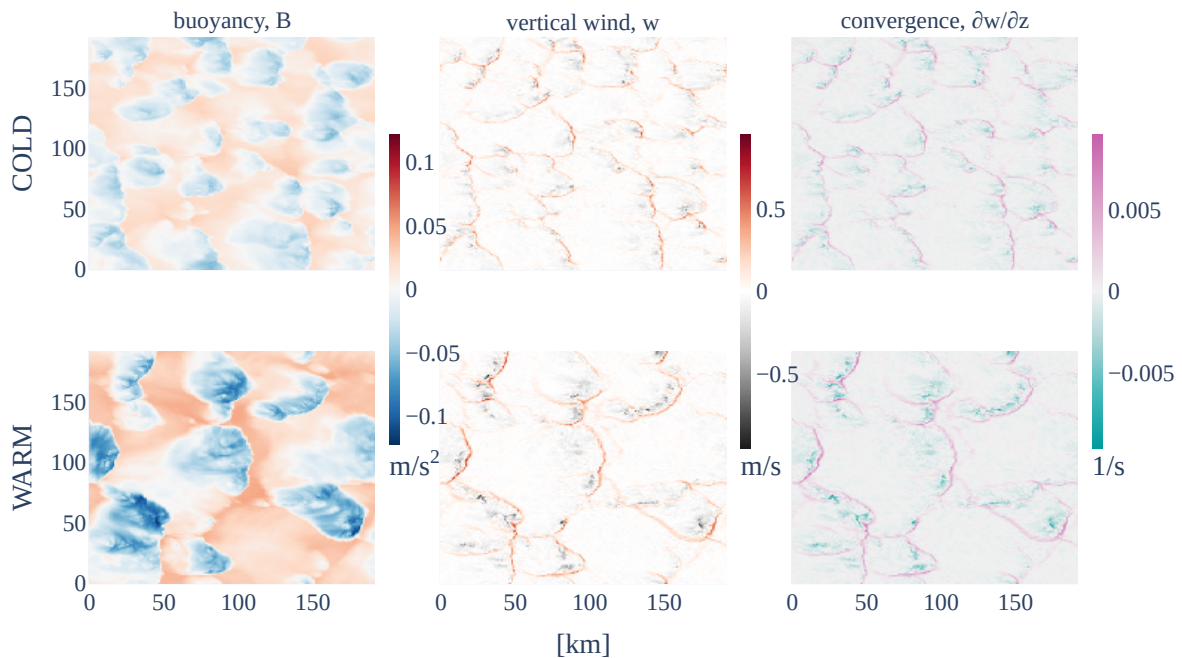
Figure 5.6: Buoyancy and convergence as drivers of updrafts. A snapshot of the entire domain is shown at simulation time 17:00 hr. The colder simulation in the top row can be compared with the invigorated values for all three variables in the warmer simulation in the bottom row. The variables B, w and $\partial w/\partial z$ each have their own colorscale to the right of their panels. In the colorbars reddish hues represent upward motion or the promotion of upward motion. The colorscale of w is chosen such that it has color similarity to what is shown in Figure 5.5

5.2.3. Contributions of buoyancy and convergence near the surface

The expanding gust fronts near the surface increase the magnitudes of horizontal convergence and divergence. Near the surface, the convergence is linearly related to the vertical motions.

The buoyancy is not clearly related to the vertical velocities in the sub-cloud layer. The relative importance of the factors in the vertical velocity described in Section 4.2 is not determined, nor is the change in magnitude of these forces with climate change determined. But the variability of convergence does explain most of the variability in vertical motion. The high coefficients of determination show a strong linear relationship between convergence and updraft velocity.

What can be seen in Figure 5.7 is that the variance of the buoyancy increases for the warmer scenario. Besides that, the distribution in the histogram becomes wider, and also more skewed to the right with a growing tail of negative values. This means the median becomes more negative. This is due to the strongly negatively buoyant points in the cold-pools. Because buoyancy is determined from a local perturbation of the slab mean, more negatively buoyant points make the other points relatively more buoyant.
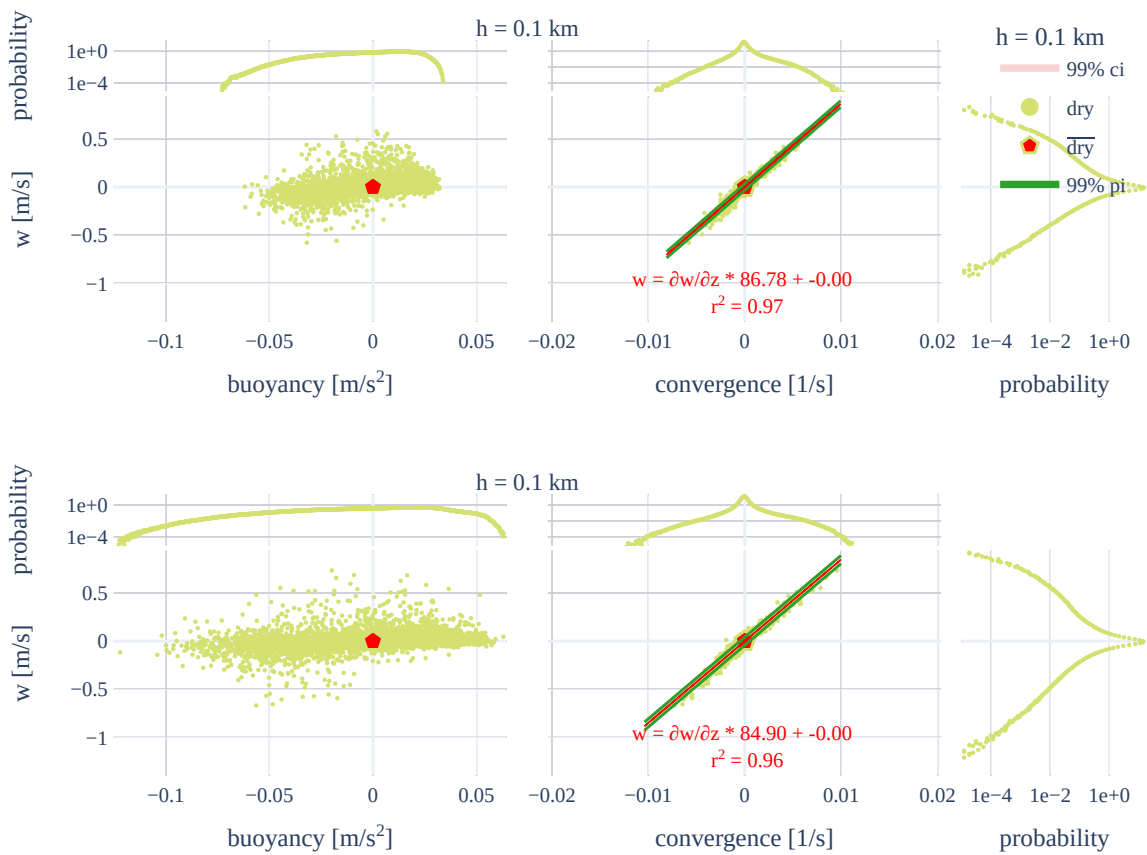
Figure 5.7: The relations of buoyancy and convergence to vertical velocity in the near-surface layer. Besides the scatter plots, empirical probability with the counted probability in a logarithmic scale are attached. Through the scatterplot of convergence an ordinary least squares regression line is estimated together with the two-tailed 99% confidence and prediction intervals. The coefficients of determination of the regression line are given as r^2

5.3. Buoyancy and convergence in the clouds

The importance of convergence near the surface was shown in Section 5.2.3. Here the importance of buoyancy in the clouds is shown.

In the simulations, there is a relationship between the buoyancy in a cloudy grid cell and its vertical velocity. Cloudy areas are on average more buoyant than their dry counterparts. The cloudy areas also have stronger upward velocities. In the warmer simulations, the magnitude of the upward velocities and the magnitude of the buoyancy perturbations increases.

In Figure 5.8, a scatter plot of buoyancy and vertical velocity is shown. A linear relationship in cloudy points between buoyancy and vertical velocity is indicated. The quality of the linear fit is determined with the coefficients of determination r^2. A higher r^2 means a better linear fit. In the cloudy cross section, horizontal convergence does not correlate to the vertical motions. This holds for the cross sections at all heights.

In the COLD simulation, the linear correlation of buoyancy to vertical velocity is lower for the layers at 5.5 km and 7.0 km (not shown here). At the same time, in tests with a lower threshold of q_c, the saturated fraction increases. With a threshold of $q_c > 0$, the cloudy fraction was bigger. This is an indication that the convection does not grow as deep, with detrainment already at lower heights. Comparing the scenarios shows that with warming, both the velocities and the buoyant accelerations increase. The clouds have more vigorous buoyant updrafts concentrated in a slightly smaller cloudy area.
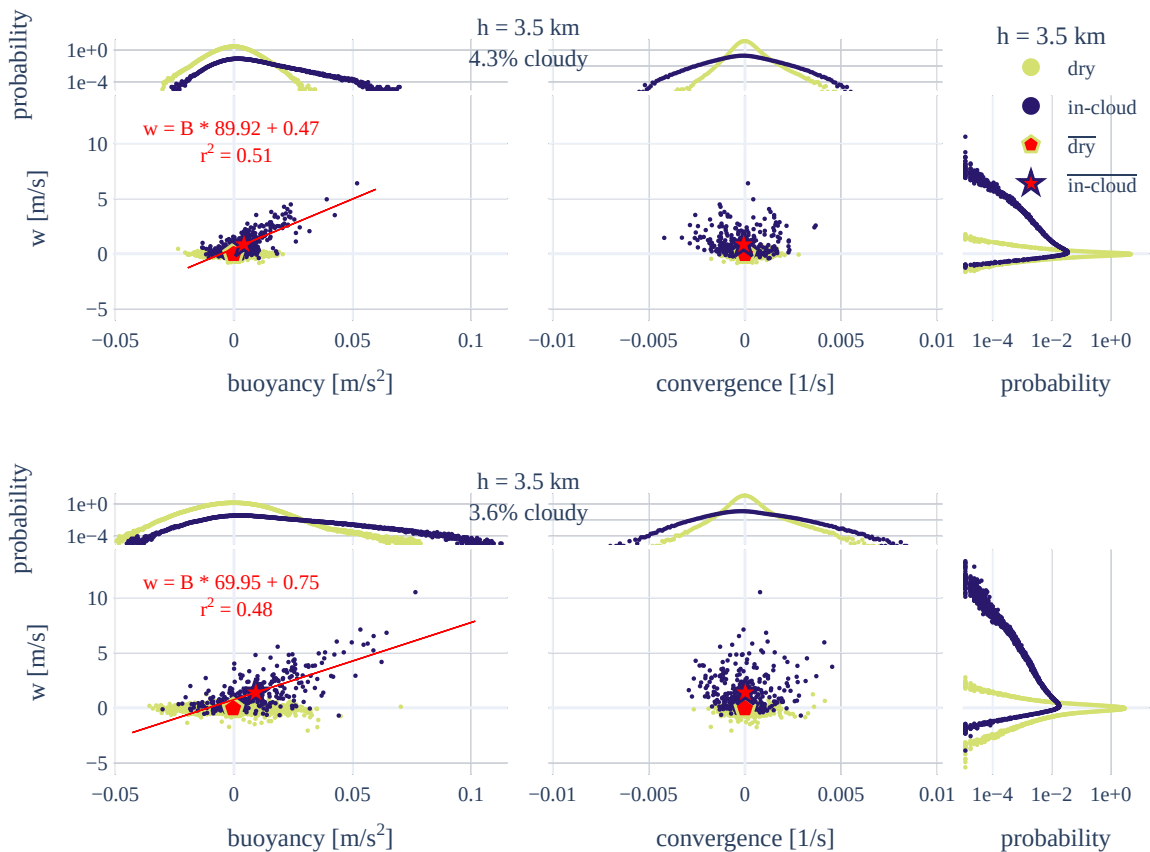
Figure 5.8: The relations of buoyancy and convergence to vertical velocity in the near surface layer. Besides the scatter plots, empirical probability with the counted probability in a logarithmic scale are attached. The cloudy percentage is number of preprocessed grid points that have $q_c > 0.1$ g/kg over the total number of points. Through the scatterplot of buoyancy an ordinary least squares regression line is estimated through the cloudy points. The coefficients of determination of the regression line are given as r^2. No confidence intervals are determined for this non-normally distributed data.

5.4. Three dimensional overview of vertical velocities

In the previous sections, results were presented per cross section. A first hint to the dynamic three dimensional relationships was implied in Figure 5.5. However, a more explicit approach is preferred to link the various cross sections together. To establish a better three dimensional picture, investigation is done into how updrafts and subsiding areas connect vertically. In Section 5.4.1, the velocities are normalized per cross section and compared between the heights. In the following sections, grid points are selected that are located directly above each other. In Section 5.4.2 this is done for cloudy columns and in Section 5.4.3 this is done for all column-wise pairs.

5.4.1. Normalized vertical velocities

Normalized vertical velocities are displayed for the 7 sections of the domain during the middle of the organized phase. These sections are zoomed into an 100x100 km part of the domain. Zooming in makes it possible to see some details in Figures 5.9 and 5.10. The normalization is performed to make structures visible on the same color scale throughout all cross sections. The velocities normalization is based on the values in the REF simulation.
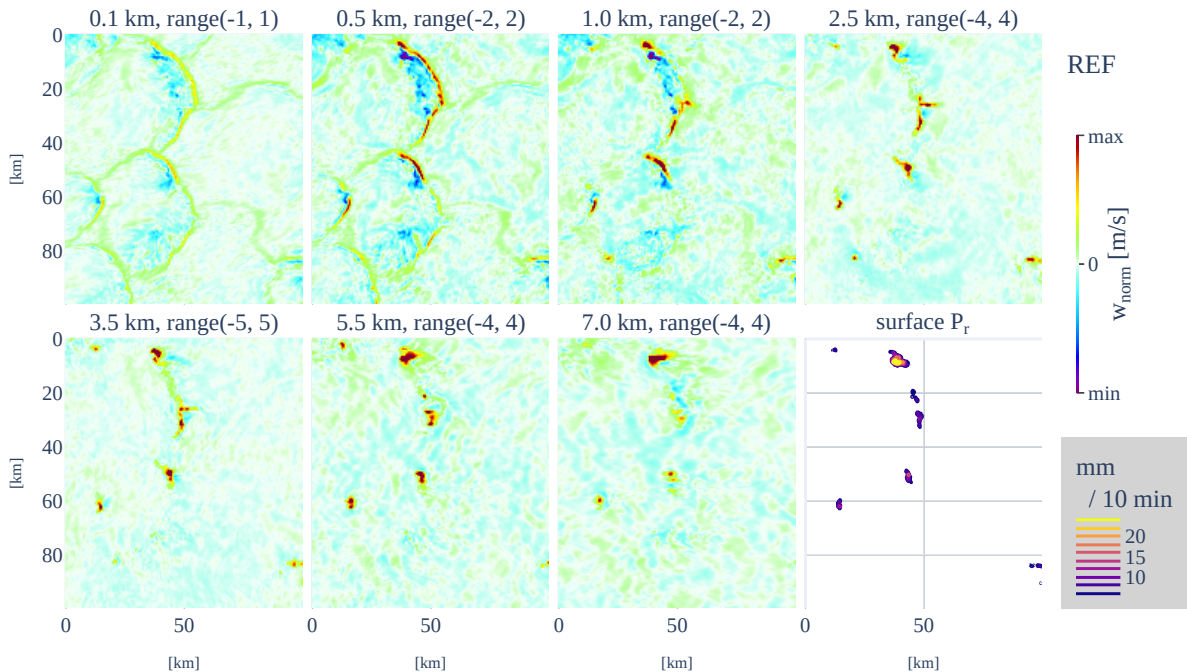
Figure 5.9: An overview of normalized vertical wind speeds in the REF simulation. A snapshot is used of part of the domain. Ranges of normalization are shown on top of each panel and similar for matching panels between the simulations. The ranges of simulation determine the maximum and the minimum color. The vertical wind speeds are normalized per layer with a symmetric range around zero. The maximum is determined by either taking the maximum of either 1 m/s or the 99.9th percentile of vertical velocity of the instantaneous filtered wind speed in the rounded to the nearest integer.

Looking at Figure 5.10, a qualitative comparison between the WARM and the COLD scenarios can be made. It can be seen that the warmer the scenario is, the more defined the updraft and subsiding structures are. In the boundary layer there are curved lines of strong updrafts, closely followed by areas of subsiding motion. This is the imprint of a cold-pool being formed by a downdraft, with rising air at the front of the outflow boundary.

Following the updrafts higher up, strong updrafts from the boundary layer extend up to the cloud in concentrated cores. The updraft cores are visible in the warmer simulations. In the WARM simulation even more so than in the REF simulation. Updraft cores are 'supported' by a spatially continuous updraft starting at the near surface layer. Updrafts are displaced with respect to the sub-cloud gust fronts. The gust fronts are visible in the lower layers. Strong updrafts that continue through the layers, reside
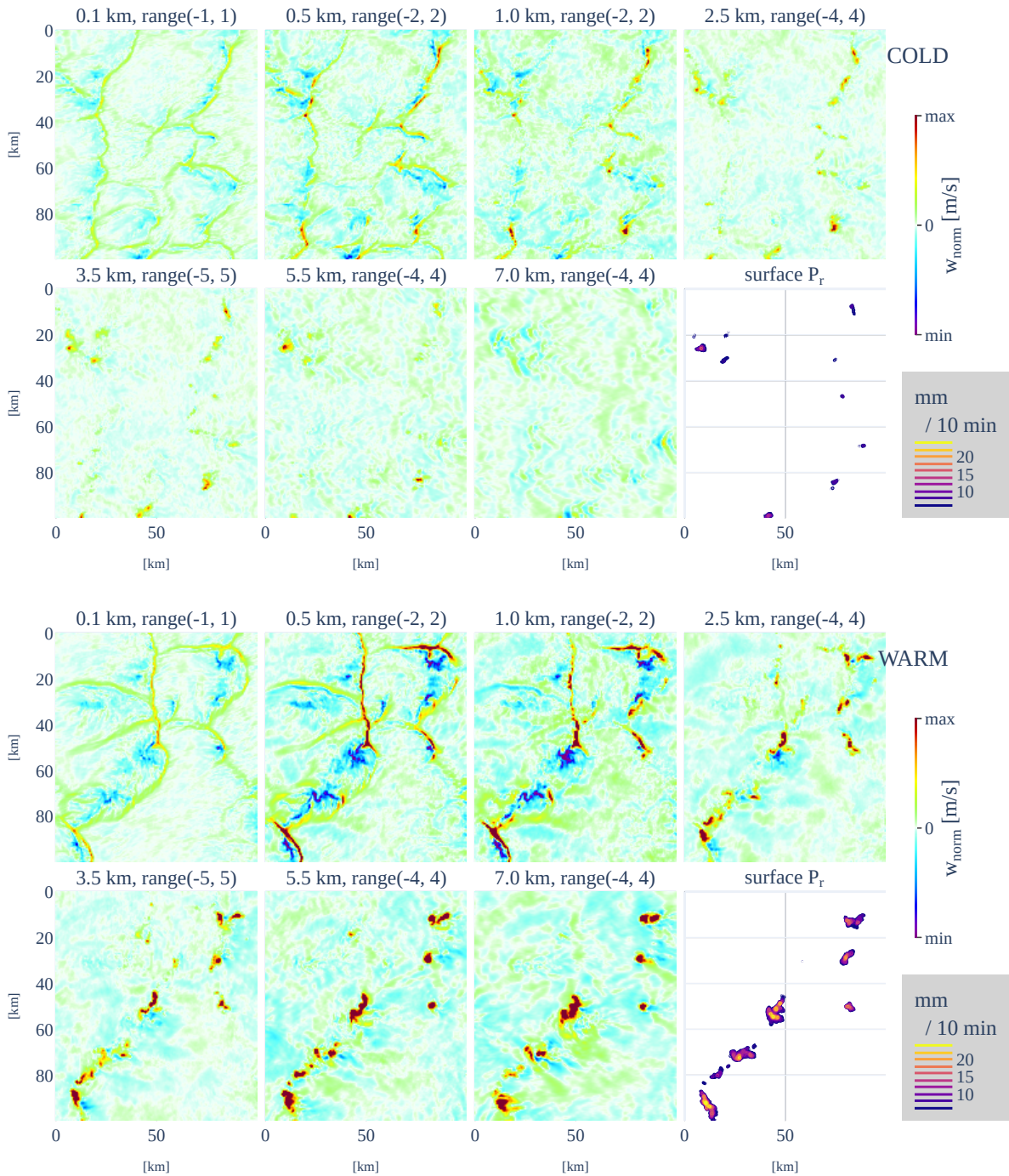
Figure 5.10: An overview of normalized vertical wind speeds in the COLD and WARM simulations. A snapshot is used of part of the domain. Ranges of normalization are shown on top of each panel and similar for matching panels between the simulations. The ranges of simulation determine the maximum and the minimum color. The vertical wind speeds are normalized per layer with a symmetric range around zero. The maximum is determined by either taking the maximum of either 1 m/s or the 99.9th percentile of vertical velocity of the instantaneous filtered wind speed in the reference scenario rounded to the nearest integer.

above downdraft regions. Such strong consistent updrafts can be seen around $x, y = (25, 70)$ km or $x, y = (50, 50)$km in WARM. This might coincide with rain from a cloud cell at a adult or late stage of its life. This cloud cell is trailing behind the updraft front that generated it and positively feeding back into it by pushing a downdraft through precipitation. A similar analysis can be made for REF with slightly less evident cold-pool structures.

5.4.2. Vertical relations within cloud columns

Vertical motion

Areas that are cloudy in subsequent cross sections generally have positive velocities in both layers. The exception to this generalization is due to the less deep convection in the colder simulations. The higher layers of the COLD simulation incidentally have negative velocities. A warmer simulation has stronger upward velocities in all the cloudy columns.

The relationships in the vertical between grid points can be seen in Figure 5.11. Since the convection is not as deep in COLD, negative velocities at the cloud tops are visible at 7 km in the rightmost panel in the bottom row. The relationship of vertical motion within the cloud columns is similar for all simulations. The coefficients of determination of the cloudy column w are similar between the different simulations. The simulations show a lack of correlations between the near-near surface layer at 1.0 km and the cloud layer at 2.5 km. At the near cloud

A stronger dependency within the cloud columns is visible between the cloud layers at 2.5 km and 3.5 km than between the other layers. The similarities between the simulations are not the case for the highest cross sections where COLD has lower updraft velocities and less cloudy points based on this threshold.

Furthermore, the distance between the cross sections can matter for the spatial relationships. The wind shear is offsetting the cloudy updrafts horizontally as they 'travel' up. This reduces spatial correlations if more distance is between the cross sections. Besides that, the linear correlation of the cloud column w near cloud base and the lowest cloud cross section is very weak as can be seen in the leftmost panels of Figure 5.11.
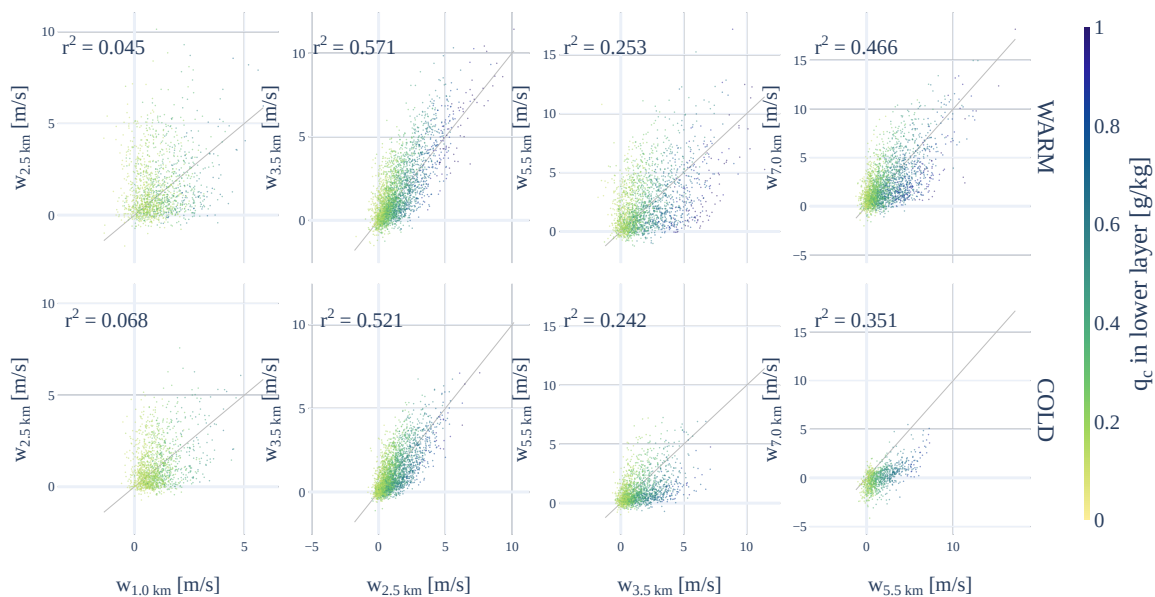
Figure 5.11: Spatial relations of vertical velocities between layers. The areas that are cloudy at the same horizontal position are selected. These grid points have their South-North and East-West location the same and have $q_c > 0.1$ g/kg in both layers. They are plotted with the vertical velocity, w, in the lower layer on the x-axis and the velocity in the upper layer on the y-axis. The coefficient of determination, r^2 of the vertical velocities at those points is given on top of each plot. This gives some information on how good the fit of a linear relation between the vertical velocities is. A helper line with $w_{lower} = w_{upper}$ is plotted in the background. Each column has a similar x-range and y-range for ease of comparison of the scenarios. Values of q_c at the lower layer are used for coloring.

Cloud water

The amount of cloud condensed water, q_c, is of importance for the updraft velocities in cloud columns. If water has already condensated, parcels have less tendency to be faster higher up in the cloud column. If water condensates during the upward motion, parcels tend to be faster higher up. This relation can be seen in the colorshift for the particles that are close to the origins in Figure 5.11. The grid cells containing less q_c in the lower layers accelerate to higher vertical velocities in the upper layers. Testing with coloring of the points with q_c in the upper layer showed an inverse acceleration result. Grid cells that contain more q_c in the upper layer tend to have higher velocities than the same grid cells in the lower layer.

5.4.3. Vertical relations in updraft columns

In the previous subsections, the updrafts at the gust front boundaries were visible in snapshots in Figures 5.10 and 5.5. Relations of these could be visually inferred. However, a more quantified approach is preferred to link the updrafts in the gust fronts tot the updrafts in the clouds. This quantification is presented here.

The vertical relations of the updraft speeds are shown in Figure 5.12. In this Figure, the vertical velocity of a layer is displayed on the x-axis and the vertical velocity of the same spatial positions in the next cross section with available data outputs. The coloring is done with the buoyant acceleration in the lower of the two layers. As an aid, also a thin grey line is plotted where the vertical velocities in the layers are equal $w_{lower} = w_{upper}$. The relation between the cross sections at 3.5 km and 5.5 km is omitted and only WARM and COLD are compared.
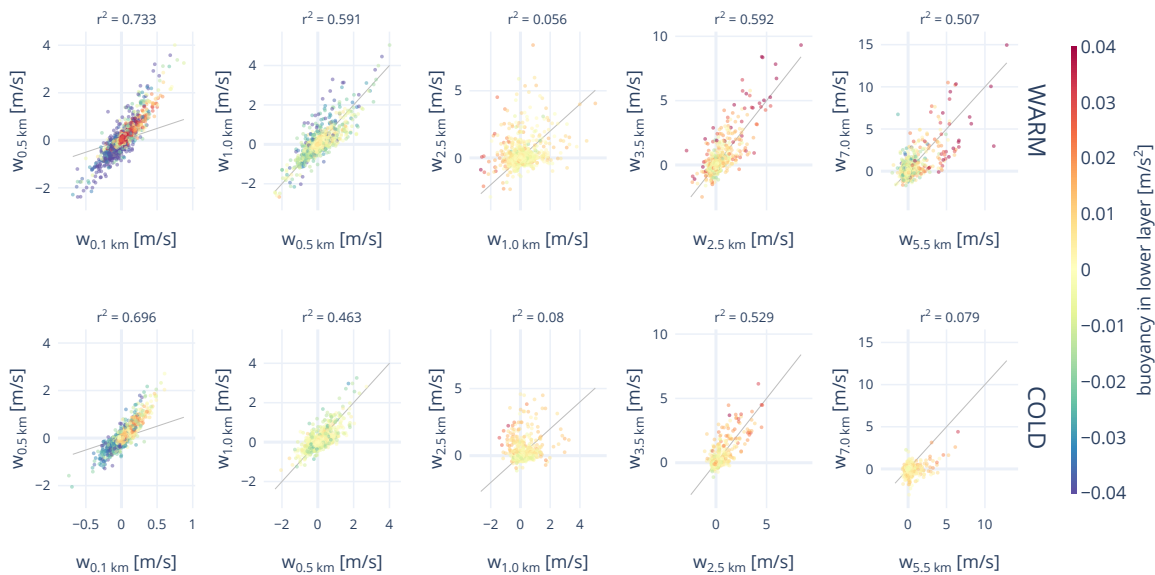
Figure 5.12: Spatial correlations of vertical velocities between layers. Buoyancy at the lower layer is used for coloring. Only columns where in both layers $q_c > 0$ are used.

The values of the coefficients of determination r^2 in Figure 5.12 are close to, but slightly different to the values found in Figure 5.11. This is because here no selection criteria are applied whilst in the previous figure only cloudy points were selected. The spatial correlations dramatically improved in all cases by the spatial filtering procedure of the preprocessing described in Section 4.6. Before filtering, the relations in the sub-cloud layers were not correlated. After the preprocessing procedure, the correlation between the near surface layer to the sub-cloud layer became the strongest with $r^2 = 0.733$ for the

WARM scenario.

Difference between WARM and COLD can be seen in the relations of the highest cloud layers. The updrafts in COLD are less vigorous and do not persist upwards to 7 km as often. This reduces the signal strength. With a lower signal to noise ratio r^2 is thus lower than in the WARM simulation.

5.5. Moisture transport into clouds

Up until here, focus has been on updrafts. But ultimately, precipitation is determined by the amount of moisture available for the formation of precipitation. Here, first the spatial structure of moisture transport is shown in Section 5.5.1. After that, a comparison is made of the tails of the probability distributions of moisture transport in Section 5.5.2. Finally, the contributions of moisture and vertical velocities to moisture transport are dissected in Section 5.5.3

5.5.1. Spatial locations of moisture transport

In updrafts the moisture transport is positive. In Figure 5.13, the moisture transport rates can be seen with isolines of precipitation overlayed for the WARM and COLD scenarios.

Higher up, the moistening updrafts align with the convective precipitation cores. Between the snapshots, a spatial relationship in the areas of positive (or negative) moist transport between the nearest layers can be inferred. The higher up, the better these moistening updrafts coincide with the precipitation cores.

The cold-pool structures are more easily seen in WARM than in COLD. In the sub-cloud layers and the near cloud base layer, the drying effect of the cold-pools can be seen around the precipitation cores. The structures visible here in the moisture transport correspond very well with the structures visible in the vertical velocities in Figure 5.10.
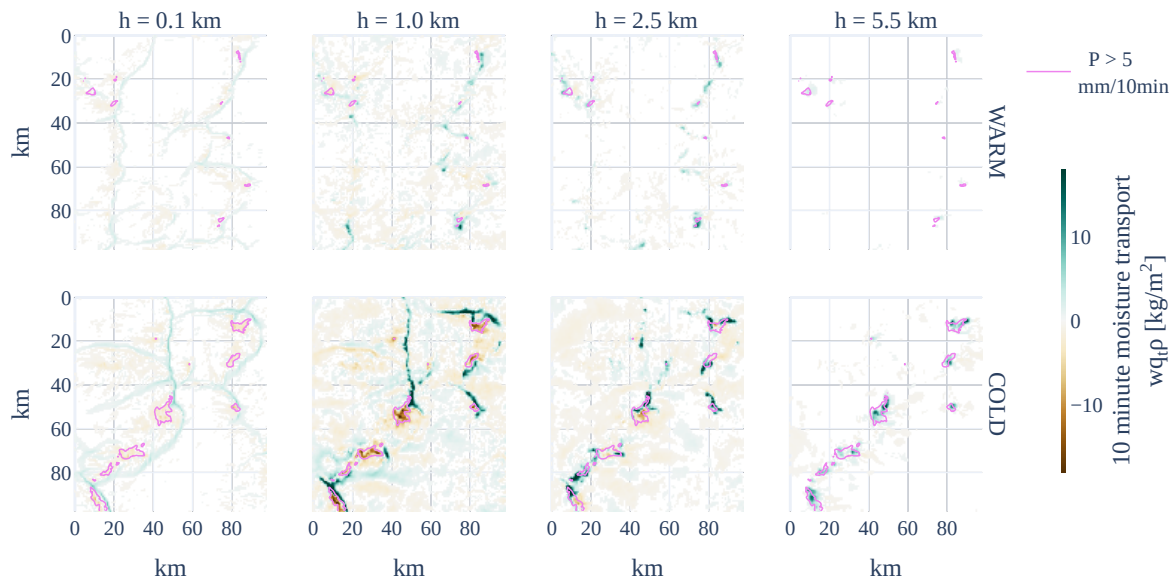
Figure 5.13: Spatial snapshot of moisture transport of part of the domain. With overlayed surface precipitation contours where precipitation is bigger than 5 mm/10min. A representative spatial snaphot in the middle of the organized phase is shown at simulation time 17:00 hour.

5.5.2. Convective cores in the probability distribution tails

Convective cores become more vigorous for a warmer simulation. The median of moisture transport values is slightly negative for all simulations. The mean of moisture transport values is positive. The moisture transport upwards is thus concentrated. These convective cores are in the positive tail of the moisture transport probability distributions. With warming of the simulation, the variability of the moisture transport increases. Furthermore, the tail of the moisture transport distributions gets stretched. In Figure 5.14, the tails of the moisture transport distributions are shown. The tails are cut off below the 99.95th percentile. Since the entire tail of the probability distribution is presented, this result is not sensitive on the percentile chosen.
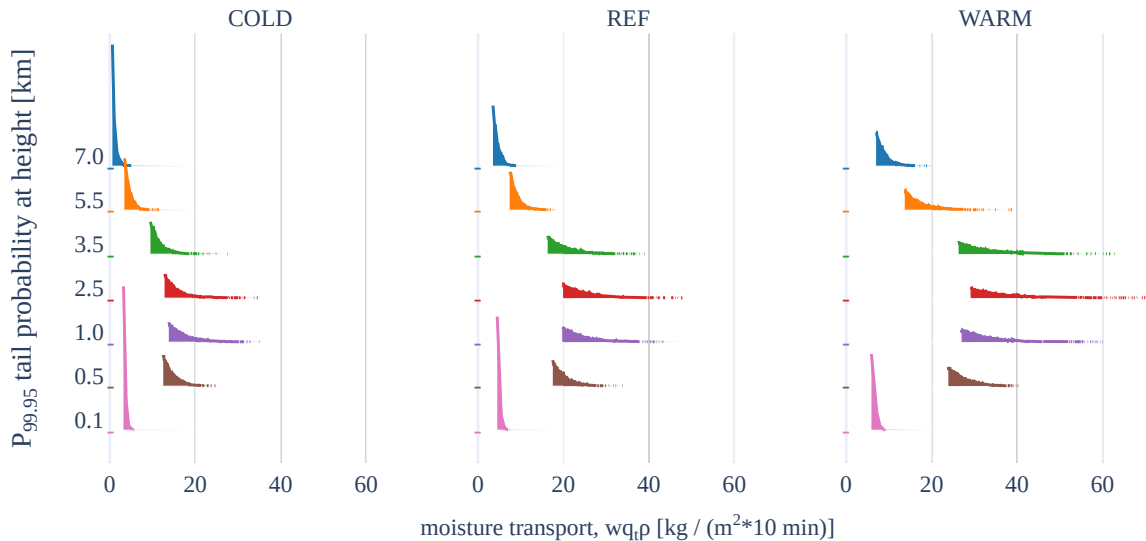
Figure 5.14: The moisture transport distributions in the tail for values higher than the 99.95th percentile in the organized phase.

5.5.3. Ingredients for moisture transport

As could be seen in Methods Section 4.1.1, the moisture transport is constructed with the vertical motion w, the total specific humidity q_t and the density of air ρ. In this Section, the secret of the chef is investigated. The contributions are deconstructed to see the pieces separately. A color scheme is adopted in which green is made from the combination of blue and yellow. That is moisture transport rate is the transporting updraft is combined with moisture content. For this, the mean rate of the filtered variables is taken per minute. These 180 mean points are collected and put into boxplots.

Absolute differences between the simulations

With warming, moisture transport in the clouds increases. The cross section at 1 km is the most transporting layer for all simulations. As the cross sections become higher, the transport decreases primarily because the amount of moisture decreases towards the troposphere. The WARM scenario has stronger variability of the domain mean parameters. This is due to the more pronounced peak of the organized phase.

To show both the moisture transport and its contributions in one visualization, the domain mean rate is taken together with the domain fraction for each timestep. It is noteworthy to remember that this could be converted to yield by multiplication of the rate with the fraction. Yield is not shown for brevity. This binning of the domain mean rates is done for precipitation at the surface as well as moisture transport after the conditional selection. These results are plotted as boxplots with whiskers that cover all outliers. This gives an overview of participating area fraction, intensity and the contributions to the

moisture transport at once. In Figure 5.15 this is shown for clouds and in Figure 5.16 for updrafts. The interquartile ranges can be recognized as the 'box' part. All values outside the interquartile range are covered by the 'whiskers'. The box plots show the spread of domain mean values per timestep in organized phase. The domain mean values are considered not to have outliers, therefore the whiskers of the boxplots are extended to cover all datapoints rather than omitting outliers.

Moisture transport is increasing everywhere in the clouds in Figure 5.15. In the blue column, it can be seen that the moisture has a positive climate scaling contribution at any time. Vertical motions generally increase more higher up in the clouds.
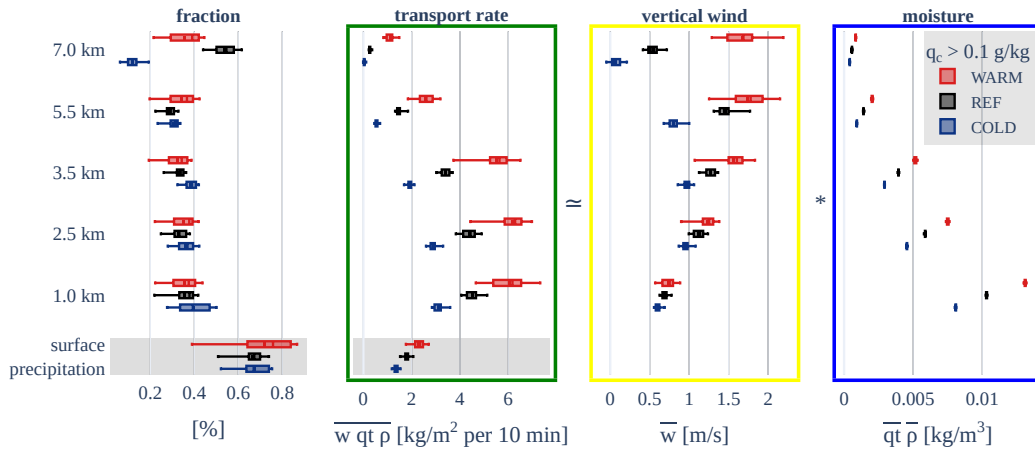
Figure 5.15: The moisture transport in the organized phase. Sampled on updrafts with cloud water > 0.1 g/kg. From left to right are four columns. In the first, the fraction of domain that is covered in clouds m^2/m^2 is shown. In the second, the domain mean moisture transport rate is shown. In the third, the vertical wind speeds within the clouds. In the fourth, the total moisture content determined from the total specific humidity multiplied with the air density is shown. In the grey box at the bottom, surface precipitation is presented as if it is moisture transport as well.

For the moisture transport in the updrafts shown in Figure 5.16, a similar result is found as for the transport in the clouds. Now the result can be extended to the updrafts stronger than 0.4 m/s in the sub-cloud layers. The transport of moisture is the strongest in updrafts in these sub-cloud layer.

The resulting moisture transport in updrafts however is sensitive to the threshold set. A lower threshold of 0.2 m/s was tested. With such a lower threshold there is no complete agreement for increasing updraft moisture transport in all the layers with warming. The tested lower threshold is not shown.

In the case shown in Figures 5.16 and 5.15, the cloud layers transport yields do still increase with warming. Rates for the COLD scenario are lower at all levels, but for WARM they are not always higher than the REF. Especially the sub-cloud layers are interesting, there the domain fraction comes into play. In both near surface as the sub-cloud layer, the domain fraction decreases for the warmer scenarios. These layers still have higher transport rates, but the yields go down due to the restrictive threshold.
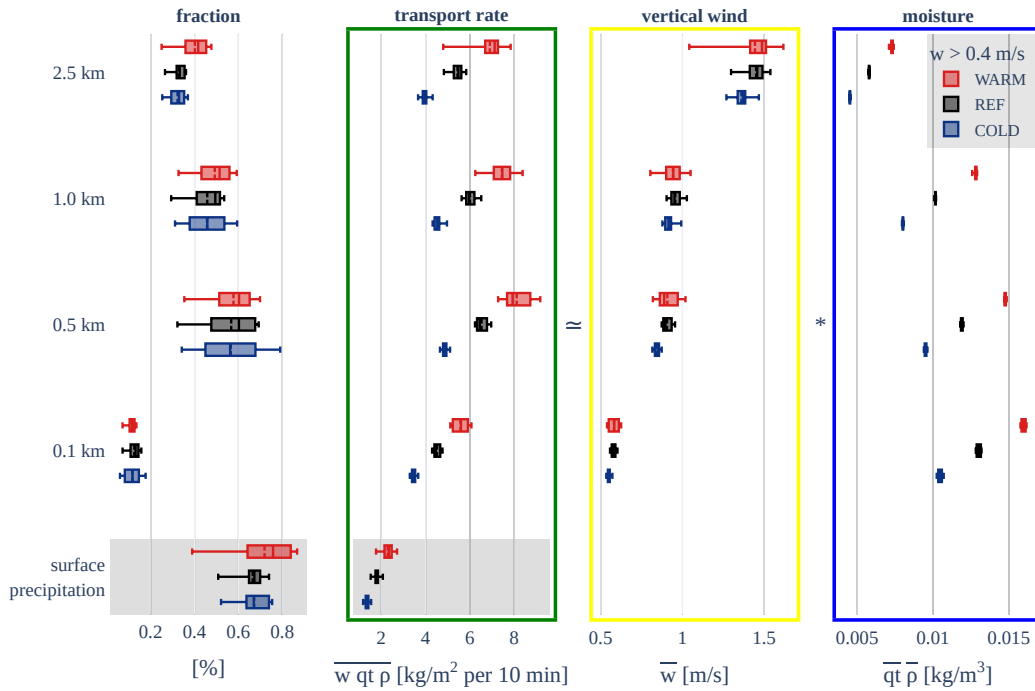
Figure 5.16: The moisture transport in updrafts in the organized phase. Sampled on w > 0.4 m/s. From left to right are four columns. In the first, the fraction of domain that is covered in updrafts m^2/m^2 is shown. In the second, the domain mean moisture transport rate is shown. In the third, the vertical wind speeds within the clouds. In the fourth, the total moisture content determined from the total specific humidity multiplied with the air density is shown. In the grey box at the bottom, surface precipitation is presented as if it is moisture transport as well.

Climate scaling of contributions

Besides the absolute differences between the simulations, the climate scaling of separate components is of interest. This is a split into thermodynamic and the dynamic contributions as described in Theoretical introduction Section 2.1.7.

The dissection into climate scaling coefficients α is presented in Figures 5.18 and 5.17. The density is assumed to not change in order to make easier comparisons in the blue moisture panel. Note that the domain fractions column is not given in α. It shows the absolute difference, similar to Figures 5.15 and 5.16.

The moisture climate scaling for strong updrafts is around or even below the CC apparent scaling. Yet in clouds, it can be higher. Especially in the upper layers. One explanation might be that due to better organization of moisture into cloud columns with warming. The scaling of the vertical wind in the strong updrafts in the sub-cloud layers is unexpected. In the sub-cloud layers, the updraft fraction does not significantly increase and the strong updraft speeds on average do not increase. It might be possible that the increase in moisture transport is purely due to the moisture climate scaling. Another possibility is that this is due to a statistical artifact from the procedure taking the domain means and comparing these per timestep.
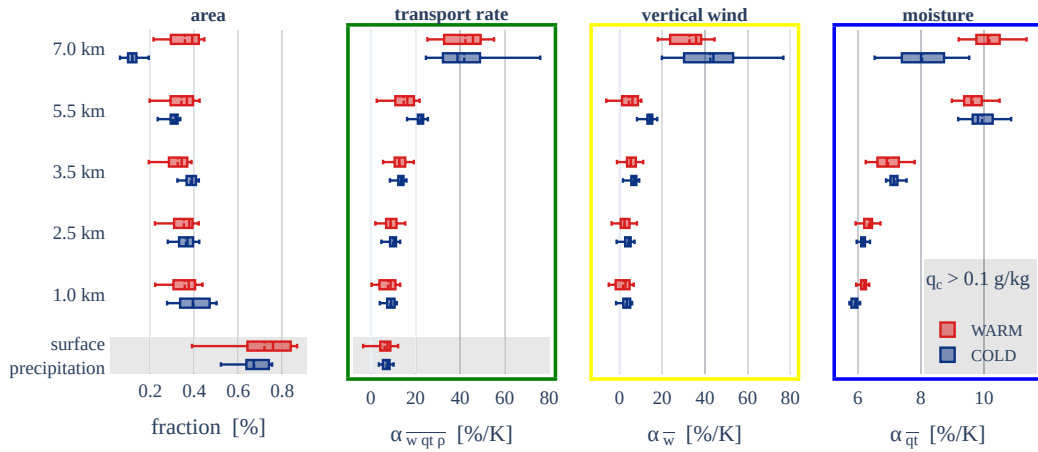
Figure 5.17: The climate scaling of moisture transport and its contributions in clouds in the organized phase. Sampled on $q_c >$ 0.1 g/kg. From left to right are four columns. In the first, the fraction of domain that is covered in clouds m^2/m^2 is shown. The fraction is not scaled with respect to the reference. In the second, the climate scaling of domain mean transport rate is shown. In the third, the climate scaling of the vertical wind speeds within the clouds. In the fourth, the climate scaling of the total moisture content. In the grey box at the bottom, surface precipitation is presented as if it is moisture transport as well. Precipitating fraction is thus not scaled, but precipitation rate is. The climate scaling coefficients α are determined per minute. Found α are summarized in boxplots containing 180 coefficients.

Figure 5.18: The climate scaling of moisture transport and its contributions in updrafts in the organized phase. Sampled on w > 0.4 m/s. From left to right are four columns. In the first, the fraction of domain that is covered in updrafts m^2/m^2 is shown. The fraction is not scaled with respect to the reference. In the second, the climate scaling of domain mean transport rate is shown. In the third, the climate scaling of the vertical wind speeds within the clouds. In the fourth, the climate scaling of the total moisture content. In the grey box at the bottom, surface precipitation is presented as if it is moisture transport as well. Precipitating fraction is thus not scaled, but precipitation rate is. The climate scaling coefficients α are determined per minute. Found α are summarized in boxplots containing 180 coefficients.

6

Discussion, conclusions and recommendations for future work

This chapter builds further upon the results in Chapter 5. To do this, first the results are summarized along the lines of the research questions. This summary is in Section 6.1. Next, a reflection is done on the quantification and importance of dynamic processes that contribute to extreme precipitation in mid-latitudes in Section 6.2. Here a conclusion is made on whether the aim of this research is reached and what the significance of the outcomes is. Following that, the limitations of this work are discussed in Section 6.3. Finally recommendations for future work are made in Section 6.4.

6.1. Summary of results

The objective of this research is to understand more about idealized extreme precipitation events in a warming climate in the Netherlands. The effects of climate change on extreme precipitation in the Netherlands are modeled using the Dutch Atmospheric Large Eddy Simulation (DALES). Atmospheric conditions from a composite of days with extreme precipitation are perturbed. The entire atmospheric temperature column is warmed and cooled by 4 degrees Kelvin whilst keeping the relative humidity constant. The possible changes to the warming and moistening of the atmosphere are modeled. The simulated outputs of the resulting COLD, REF and WARM scenarios are critically evaluated. A period of 3 hours of organized convection in the simulations was selected for comparison between them. In this period of extreme precipitation, the yield amount increases 8.5% per degree Kelvin. Processes that ultimately determine the intensity of precipitation are dissected along the lines of sub-questions. The sub-questions are listed below here to structure this summary of results.

A. Updrafts in the clouds

In a warming atmosphere over the Netherlands how are updrafts in the clouds changing?

Updrafts in the clouds become stronger with climate warming. The updrafts at 3.5 km height are most representative of precipitation yield. These updrafts increase in velocity by 4.7% per degree Kelvin. Cloudy updrafts penetrate higher into the atmosphere. The convection grows deeper. The increase of updraft strength is greater higher up in the clouds. At 7 km height, updraft speeds increase up to 20.7 % per degree Kelvin. The response with two pronounced phases of precipitation during the day is also present in the updrafts. The two-phased response is stronger in the warmer scenario.

B. Moisture transport into the clouds

In a warming atmosphere over the Netherlands how is the moisture transportation into the clouds changing?

Most moisture transport occurs low in the clouds at 2.5 km height and near cloud base at 1 km. This is the case for all used simulations. With warming, more moisture is transported higher up in the 3.5 km cloud layer than near cloud base. The area of clouds and updrafts that transport moisture increases with warming in the cloud layers, except at 7 km. At this height, the area fraction of clouds and updrafts decreases with warming. But the mean upward speed and cloud moisture increase leading to a 10% higher transport rate in both clouds and updrafts. The deeper convection concentrates the moisture transport into small towering areas.

In general, the least moisture transport happens in the near surface layer at 0.1 km. Moisture transport near the surface increases along organized gust front lines. On average the increase in transport by updrafts in the sub-cloud layers is dominated by increased moisture rather than due to strong updrafts becoming stronger. Parts of these gustfronts persist to higher altitudes. More moisture is transported higher up into the clouds. The moisture that is concentrated into convective cores coincides with intenser precipitation cores. Around and in the precipitating cores the air in the sub-cloud layers undergoes a drying effect.

C. Cold-pools, gust fronts and the link to updrafts in the clouds

In a warming atmosphere over the Netherlands what is the influence of cold-pool associated sub-cloud gust fronts on updrafts in the clouds?

In the reference situation, cold-pools are already present. With warming the subsiding motion accelerates and a stronger drying effect is present around precipitation cores. Buoyancy perturbations in the sub-cloud layers are increased, giving cold-pools more strength. The cold-pools become larger, with bigger gust front structures. Relations between the gust front structures and the convective cloud cores is inferred visually. The vertical motions in the near surface layer can be linked directly upwards to vertical motions in the subcloud layer. This is done in the WARM simulation with a coefficient of determination of $r^2 = 0.733$. Consequently, the motions in the sub-cloud layer can be linked directly upwards with $r^2 = 0.591$. The link between the near cloud base layer at 1 km and the lower cloud layer is not related with $r^2 = 0.056$. Wind shear is present. Horizontal displacements due to win shear can deteriorate the relations between layers. No corrections are applied for the wind shear. The layers relate better to each other in the WARM simulation than in the COLD simulation.

6.2. Conclusion

The aim of this research is to determine and quantify the importance of dynamic processes that contribute to the scaling of extreme precipitation in mid-latitudes. The aim is to help better understand how extreme precipitation in the Netherlands will intensify in a warmer climate.

In order to fulfill the aim, seperate aspects of the dynamics are critically evaluated and quantified with respect to warming. Vertical upward motions in the clouds and subsiding motions are invigorated. The clouds reach up to greater heights in a warmer simulation. Moisture transport is increased due to the increased moisture availability. In the clouds moisture transport is further enhanced by stronger updraft velocities. In the sub-cloud layers, convection is better organized into gust fronts due to cold-pool dynamics.

The hypothesis that updrafts in the clouds increase in strength is confirmed. Above cloud base the updrafts become more vigorous.

For the hypothesized feedback loop, the scaling is quantified or critically evaluated. Parts of the loop and how they are addressed are listed here.

- The increase in strength of updrafts in the clouds is quantified.
- Climate scaling of precipitation is quantified.
- The increase in strength of downdrafts is quantified.
- The relation of cold-pool strength to warming is not quantified since this was already done in Lochbihler et al. (2021).
- The relation between convergence at the gust front and updraft velocities is shown.
- The link between updrafts in the gust fronts and updrafts in the clouds is made plausible visually in snapshots. It can not be confirmed with vertical column due to wind shear.

The significance of this work is in the proposed feedback loop. The proposed feedback loop can be considered a framework to use in future studies. This framework can be used in future studies to evaluate the dynamic contribution to scaling of extreme precipitation.

6.3. Limitations of this work

- Constant column warming is assumed for the climate perturbations, the set of climate scenario's used is not as extensive as in Lochbihler et al. (2021).
- The microphysics scheme does not take into account the latent heat of freezing, which provides an extra source of kinetic energy for rising updrafts and would thus allow for deeper convection. Furthermore melting layer dynamics which would generate additional downdrafts in the clouds are not taken into account. (Böing, Steven et al., 2012)
- There are several reasons why precipitation extremes may not scale with atmospheric water vapor content. For example, the strength of circulations does not need to stay constant as climate changes. (O'Gorman & Schneider, 2009)
- The wind shear is important for how deep convection grows. Consequently, the development of cold-pools depends on the set wind shear. (Helfer & Nuijens, 2021) Only one case with strong shear is used in this work.
- Only a single model set up is used. The model setup is an idealized case. Several aspects of idealizations that constrain the general applicability are listed below.
  - Radiative heating and cooling is prescribed and not interactively diagnosed. It is assumed that radiative feedback on the daily time scale are not dominant, but this assumption may need reconsideration.

– There is no rotation in the input wind profile in the simulation. Only one specific model setup wind unidirectional shear is used.
– The surface is represented as a homogeneous flat plate without topography.
– The change of the microphysics contribution to scaling is not taken into account.

6.4. Recommendations for future research

In this section, recommendations for future work are made based on this work. First, a general recommendation is made to use LES modelling to improve parameterizations of courses models is made in Section 6.4.1. This recommendation can be applicable to the specific recommendations that follow. After this, in Section 6.4.2 the second recommendation specifically proposes the usage of LES to improve entraining plume model parameterizations. The next specific recommendation in Section 6.4.3 is about the vertical velocity budget. A recommendation is made on how to rank and quantify the importance of buoyancy and convergence for vertical accelerations. A final specific recommendation is provided in Section 6.4.4 on how to make the link between the updrafts in near surface gust fronts and updraft in clouds. Finally some minor practical advices are given.

6.4.1. Improving extreme precipitation parameterizations in forecast models

Climate models and Numerical Weather Prediction (NWP) models use parameterizations to represent processes that happen on finer scales than they can resolve. These parameterizations should be optimized for the most accurate predictions. Using Large Eddy Simulation (LES), the processes and parameters determining extreme precipitation response can be quantified. With quantification of parameters, they can be used in improved parameterization schemes to improve predictions of extreme precipitation. This is a more general idea that should always be the overarching aim of LES studies geared towards application.

6.4.2. Defining cloud cells and quantifying entrainment in cloud columns

Software for clustering cloud cells on certain thresholds already exists or can be produced. This software may be easily used to find what the climate scaling of the lateral entrainment of moisture into clouds is. Such work would continue on the work of Loriaux et al., 2013. The work of Loriaux et al. was limited by the usage of an entraining plume. Using LES is then removed. The aim of such a research would be to better quantify the contribution of lateral entrainment to super-CC scaling of (sub-)hourly precipitation extremes. With the found entrainment rates of cloud cells, the parameterizations in operational NWP or other models might be optimized.

6.4.3. Solving the vertical velocity equation with pressure perturbations

The spatial outputs available from DALES did not include pressure perturbations. This made solving the vertical velocity equation impossible. Solving the vertical velocity equation explicitly can give answers to questions about what is driving updrafts. Both in the sub-cloud layer and in the clouds, it might be interesting to know what is driving updrafts. Predominantly in the subcloud layer there is a mismatch in the orders of magnitude of the integrated acceleration by buoyancy and convergence. This mismatch might be explained by pressure perturbations. Getting a full budget of vertical forces (accelerations) makes quantifying and ranking the importance of aspects such as buoyancy and convergence for the climate scaling of updrafts feasible.

In future simulations, outputting the pressure at the cross sections would make it possible to investigate the relative importance of buoyancy, convergence and pressure perturbations in the generation of updrafts.

Furthermore, buoyancy is retrieved from the perturbation of virtual potential temperature Θ'_v from the

entire domain cross section mean. Perhaps taking a smaller area to calculate the perturbation from would give better results. This could be achieved by finding out what the typical length scale is where the Θ_v field influences a parcels tendency to rise or descend. This typical length could be used as the cutoff length of a spatial filter and then subtracted from the provided Θ_v'. This is shown in Eq. 6.1 where $< ... >_L$ represents the filter of size L.

$$B = \frac{g}{\Theta_{v,0}}(\Theta_v' - < \Theta_v' >_L) \tag{6.1}$$

6.4.4. The causal relation between gust fronts and cloudy updrafts

In the proposed framework of a feedback loop is the link between updrafts in gustfronts and updrafts in the clouds. This link should be quantified to solidify the feedback loop framework. Due to strong wind shear, this link lacks a rigorous quantification. A question one could ask themselves is how much does updraft strength in the clouds relate to updrafts in the subcloud layer. Knowledge about the link between updraft gustfronts and the in cloud updrafts can be improved in two ways.

1. By defining a mask at the near-surface layer from updrafts exceeding a certain threshold. This mask is translated vertically to a next cross-section whilst shifting the masked positions horizontally. The horizontal shift compensates for the wind shear. Perhaps the gust front propagation speed can be included in horizontal position corrections of the mask as well. This can be used to see if all updrafts in the clouds can be related back to the convergence at the surface gustfront through a translation in time and space.
2. Using particle tracking.

Since not all surface updrafts penetrate through the convection inhibiting layer, this approach can also be reversed starting at the updrafts in the clouds and translating their masked positions through time and spatial position to see if they are located above gustfronts.

6.4.5. Minor practical recommendations

Some minor practical recommendations for atmospheric scientists are listed here. These might not be interesting for the average reader, whom may consider skipping this paragraph.

- The used version of DALES calls the sum of ice and liquid water in it's outputs 'liquid water', q_l. Although it does incorporate ice effects as explained in the appendix of Böing, Steven et al. (2012), the output variable name giving can be confusing.
- The atmospheric science community is sometimes imprecise with naming of water phase fractions. The name condensed water is used for the sum of ice and liquid fractions. In basic chemistry condensation refers to the phase change of solid to liquid, thus implying that condensed water is liquid. It is recommended for atmospheric scientists to consider adopting the name of non-vapor water, since that implies all other forms of water than water vapor.
- Within the atmospheric science community, jargon is rampant. Within this work it was unfeasible to remain free of jargon. For science communication and outreach purposes, it is recommendable to keep the use of jargon to a minimum.

References

Abbott, T. H., Cronin, T. W., & Beucler, T. (2020). Convective dynamics and the response of precipitation extremes to warming in radiative–convective equilibrium. *Journal of the Atmospheric Sciences*, *77*(5), 1637–1660. https://doi.org/10.1175/jas-d-19-0197.1

Bao, J., Sherwood, S. C., Alexander, L. V., & Evans, J. P. (2017). Future increases in extreme precipitation exceed observed scaling rates. *Nature Climate Change*, *7*(2), 128–132. https://doi.org/10.1038/nclimate3201

Beard, K. V., & Chuang, C. (1987). A new model for the equilibrium shape of raindrops. *Journal of the Atmospheric Sciences*, *44*(11), 1509–1524. https://doi.org/10.1175/1520-0469(1987)044<1509:anmfte>2.0.co;2

Bentvelsen, F., Lenderink, G., & Siebesma, P. (2021). The role of updrafts in the scaling of extreme precipitation in mid-latitudes. https://doi.org/10.5194/egusphere-egu21-13571

Böing, S. (2016). An object-based model for convective cold pool dynamics. *Mathematics of Climate and Weather Forecasting*, *2*(1). https://doi.org/10.1515/mcwf-2016-0003

Böing, Steven, Jonker, H. J. J., Siebesma, A. P., & Grabowski, W. W. (2012). Influence of the subcloud layer on the development of a deep convective ensemble. *Journal of the Atmospheric Sciences*, *69*(9), 2682–2698. https://doi.org/10.1175/jas-d-11-0317.1

Chan, S. C., Kendon, E. J., Roberts, N. M., Fowler, H. J., & Blenkinsop, S. (2015). Downturn in scaling of UK extreme rainfall with temperature for future hottest days. *Nature Geoscience*, *9*(1), 24–28. https://doi.org/10.1038/ngeo2596

Feng, Z., Hagos, S., Rowe, A. K., Burleyson, C. D., Martini, M. N., & Szoeke, S. P. (2015). Mechanisms of convective cloud organization by cold pools over tropical warm ocean during the AMIE/DYNAMO field campaign. *Journal of Advances in Modeling Earth Systems*, *7*(2), 357–381. https://doi.org/10.1002/2014ms000384

Fournier, M. B., & Haerter, J. O. (2019). Tracking the gust fronts of convective cold pools. *Journal of Geophysical Research: Atmospheres*, *124*(21), 11103–11117. https://doi.org/10.1029/2019jd030980

Fuglestvedt, H. F., & Haerter, J. O. (2020). Cold pools as conveyor belts of moisture. *Geophysical Research Letters*, *47*(12). https://doi.org/10.1029/2020gl087319

Glickman, T., & Zenk, W. (2000). *Glossary of meteorology*. Boston, ARRAY(0xda23cac). http://oceanrep.geomar.de/6557/

Guichard, F., Petch, J., Redelsperger, J.-L., Bechtold, P., Chaboureau, J.-P., Cheinet, S., Grabowski, W., Grenier, H., Jones, C., Köhler, M., Piriou, J.-M., Tailleux, R., & Tomasini, M. (2004). Modelling the diurnal cycle of deep precipitating convection over land with cloud-resolving models and single-column models. *Quarterly Journal of the Royal Meteorological Society*, *130*(604). https://doi.org/10.1256/qj.03.145

Haerter, J. O. (2019). Convective self-aggregation as a cold pool-driven critical phenomenon. *Geophysical Research Letters*, *46*(7), 4017–4028. https://doi.org/10.1029/2018gl081817

Haerter, J. O., & Schlemmer, L. (2018). Intensified cold pool dynamics under stronger surface heating. *Geophysical Research Letters*. https://doi.org/10.1029/2017gl076874

Helfer, K. C., & Nuijens, L. (2021). The morphology of simulated trade-wind convection and cold pools under wind shear. *Journal of Geophysical Research: Atmospheres*. https://doi.org/10.1029/2021jd035148

Heus, T., van Heerwaarden, C. C., Jonker, H. J. J., Siebesma, A. P., Axelsen, S., van den Dries, K., Geoffroy, O., Moene, A. F., Pino, D., de Roode, S. R., & de Arellano, J. V.-G. (2010). Formulation of the dutch atmospheric large-eddy simulation (DALES) and overview of its applications. *Geoscientific Model Development*, *3*(2), 415–444. https://doi.org/10.5194/gmd-3-415-2010

Houze, R. A. J. (2014). *Cloud dynamics*.

Lenderink, G., Barbero, R., Loriaux, J. M., & Fowler, H. J. (2017). Super-clausius–clapeyron scaling of extreme hourly convective precipitation and its relation to large-scale atmospheric conditions. *Journal of Climate*, *30*(15), 6037–6052. https://doi.org/10.1175/jcli-d-16-0808.1

Lenderink, G., & Attema, J. (2015). A simple scaling approach to produce climate scenarios of local precipitation extremes for the netherlands. *Environmental Research Letters*, *10*(8), 085001. https://doi.org/10.1088/1748-9326/10/8/085001

Lenderink, G., de Vries, H., Fowler, H. J., Barbero, R., van Ulft, B., & van Meijgaard, E. (2021). Scaling and responses of extreme hourly precipitation in three climate experiments with a convection-permitting model, *379*(2195), 20190544. https://doi.org/10.1098/rsta.2019.0544

Lenderink, G., & Fowler, H. J. (2017). Understanding rainfall extremes. *Nature Climate Change*, *7*(6), 391–393. https://doi.org/10.1038/nclimate3305

Lenderink, G., & van Meijgaard, E. (2008). Increase in hourly precipitation extremes beyond expectations from temperature changes. *Nature Geoscience*, *1*(8), 511–514. https://doi.org/10.1038/ngeo262

Lenderink, G., & van Meijgaard, E. (2010). Linking increases in hourly precipitation extremes to atmospheric temperature and moisture changes. *Environmental Research Letters*, *5*(2), 025208. https://doi.org/10.1088/1748-9326/5/2/025208

Lochbihler, K., Lenderink, G., & Siebesma, A. P. (2019). Response of extreme precipitating cell structures to atmospheric warming. *Journal of Geophysical Research: Atmospheres*. https://doi.org/10.1029/2018jd029954

Lochbihler, K., Lenderink, G., & Siebesma, A. P. (2021). Cold pool dynamics shape the response of extreme rainfall events to climate change. *Journal of Advances in Modeling Earth Systems*, *13*(2). https://doi.org/10.1029/2020ms002306

Loriaux, J. M., Lenderink, G., De Roode, S. R., & Siebesma, A. P. (2013). Understanding convective extreme precipitation scaling using observations and an entraining plume model. *Journal of the Atmospheric Sciences*, *70*(11), 3641–3655. https://doi.org/10.1175/jas-d-12-0317.1

Loriaux, J. M., Lenderink, G., & Siebesma, A. P. (2017). Large-scale controls on extreme precipitation. *Journal of Climate*, *30*(3), 955–968. https://doi.org/10.1175/jcli-d-16-0381.1

Loriaux, J. M., Lenderink, G., & Siebesma, A.P. (2016). Composite case of conditions leading to high peak precipitation intensities in the netherlands. TU Delft. https://doi.org/10.4121/UUID:E066B7F5-F83B-406B-93E8-6BA3EB3659EB

Meyer, B., & Haerter, J. O. (2020). Mechanical forcing of convection by cold pools: Collisions and energy scaling. *Journal of Advances in Modeling Earth Systems*, *12*(11). https://doi.org/10.1029/2020ms002281

Molthan, A. L., & Colle, B. A. (2012). Comparisons of single- and double-moment microphysics schemes in the simulation of a synoptic-scale snowfall event. *Monthly Weather Review*, *140*(9), 2982–3002. https://doi.org/10.1175/mwr-d-11-00292.1

Mrowiec, A. A., Rio, C., Fridlind, A. M., Ackerman, A. S., Genio, A. D. D., Pauluis, O. M., Varble, A. C., & Fan, J. (2012). Analysis of cloud-resolving simulations of a tropical mesoscale convective system observed during TWP-ICE: Vertical fluxes and draft properties in convective and stratiform regions. *Journal of Geophysical Research: Atmospheres*, *117*(D19), n/a–n/a. https://doi.org/10.1029/2012jd017759

Muller, C. J., O'Gorman, P. A., & Back, L. E. (2011). Intensification of precipitation extremes with warming in a cloud-resolving model. *Journal of Climate*, *24*(11), 2784–2800. https://doi.org/10.1175/2011jcli3876.1

Muller, C. J., & Takayabu, Y. (2020). Response of precipitation extremes to warming: What have we learned from theory and idealized cloud-resolving simulations, and what remains to be learned? *Environmental Research Letters*, *15*(3), 035001. https://doi.org/10.1088/1748-9326/ab7130

North, G. R., & Erukhimova, T. L. (2009). Air and water. In *Atmospheric thermodynamics* (pp. 99–133). Cambridge University Press. https://doi.org/10.1017/cbo9780511609695.006

O'Gorman, P. A. (2015). Precipitation extremes under climate change. *Current Climate Change Reports*, *1*(2), 49–59. https://doi.org/10.1007/s40641-015-0009-3

O'Gorman, P. A., & Schneider, T. (2009). Scaling of precipitation extremes over a wide range of climates simulated with an idealized GCM. *Journal of Climate*, *22*(21), 5676–5685. https://doi.org/10.1175/2009jcli2701.1

Pendergrass, A. G. (2020). Changing degree of convective organization as a mechanism for dynamic changes in extreme precipitation. *Current Climate Change Reports*, *6*(2), 47–54. https://doi.org/10.1007/s40641-020-00157-9

Singleton, A., & Toumi, R. (2012). Super-clausius-clapeyron scaling of rainfall in a model squall line. *Quarterly Journal of the Royal Meteorological Society*, *139*(671), 334–339. https://doi.org/10.1002/qj.1919

Sui, C.-H., Li, X., & Yang, M.-J. (2007). On the definition of precipitation efficiency. *Journal of the Atmospheric Sciences*, *64*(12), 4506–4513. https://doi.org/10.1175/2007jas2332.1

Tompkins, A. M. (2001). Organization of tropical convection in low vertical wind shears: The role of cold pools. *Journal of the Atmospheric Sciences*, *58*(13). https://doi.org/10.1175/1520-0469(2001)058<1650:ootcil>2.0.co;2

Trenberth, K. E., Dai, A., Rasmussen, R. M., & Parsons, D. B. (2003). The changing character of precipitation. *Bulletin of the American Meteorological Society*, *84*(9), 1205–1218. https://doi.org/10.1175/bams-84-9-1205

Wang, P. K. (2013). Bulk thermodynamic equilibrium among water vapor, liquid water, and ice. In *Physics and dynamics of clouds and precipitation* (pp. 86–106). Cambridge University Press. https://doi.org/10.1017/cbo9780511794285.005

Zuidema, P., Torri, G., Muller, C., & Chandra, A. (2017). A survey of precipitation-induced atmospheric cold pools over oceans and their interactions with the larger-scale environment. *Surveys in Geophysics*, *38*(6), 1283–1305. https://doi.org/10.1007/s10712-017-9447-x

A

Climate scaling of strong updrafts

A.1. Timeseries of strong updrafts in the clouds

Selected strong updrafts in cloudy layers are displayed here. The organized phase is marked in dark grey. Climate scaling coefficients α_w are determined with respect to the organized phase mean values. Coefficients of determination r^2 are determined on the timeperiod marked in light grey near the vertical axis origin. The difference between the α shows the sensitivity to the chosen combination of percentile and height of the cross section.

Figure A.1 displays the most extreme climate scaling with 20.7 % per Kelvin for the simulation warming 4 Kelvin from the reference simulation. This is above the 'sweet spot' as described in Section 5.1.4. Nonetheless, the coefficient of determination r^2 for the Climate scenario with 4 Kelvin warming compared to REF of the initial vertical atmospheric profile simulation is 0.95.

Figures A.2, A.3 and A.4 display the time-response in the 'sweet spot'.
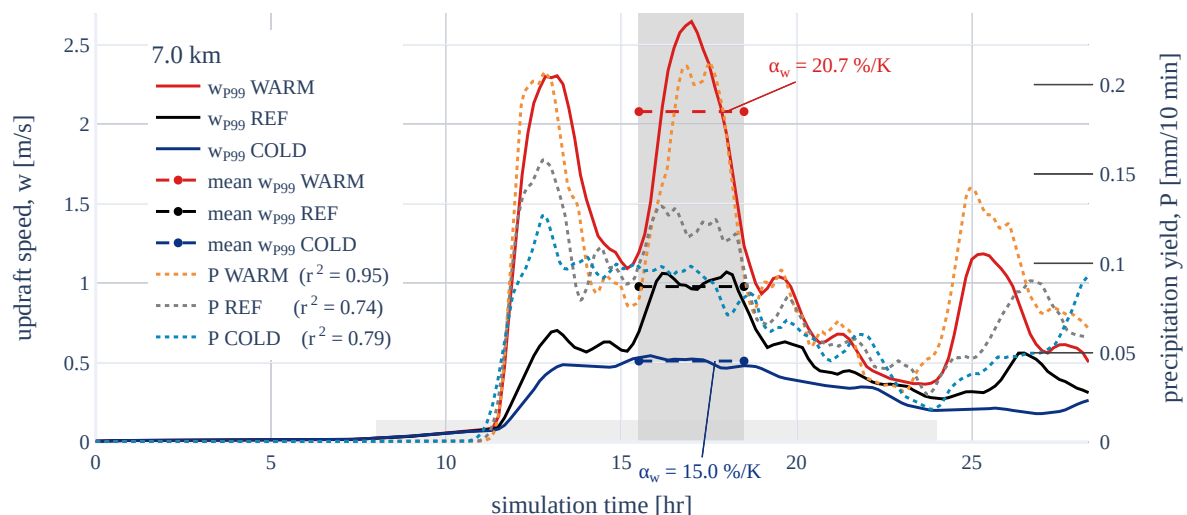
Figure A.1: Strong updrafts selected with the 99th percentile of vertical speeds in a cross section at 7.0 km.
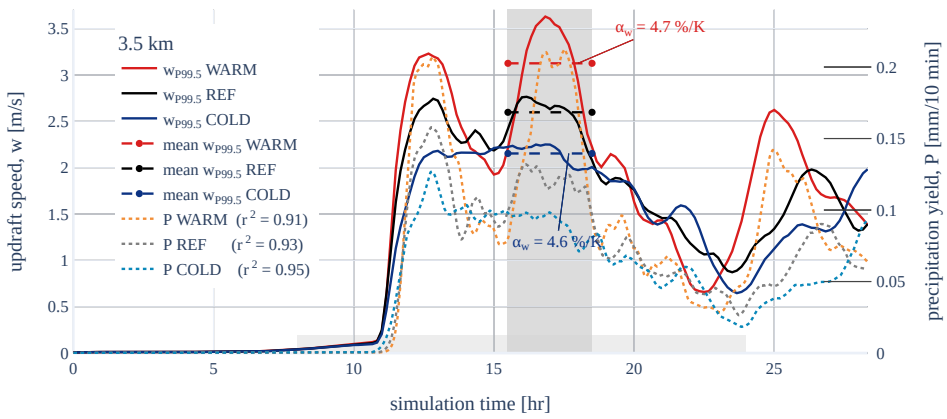
Figure A.2: Strong updrafts selected with the 99.5th percentile of vertical speeds in a cross section at 5.5 km.
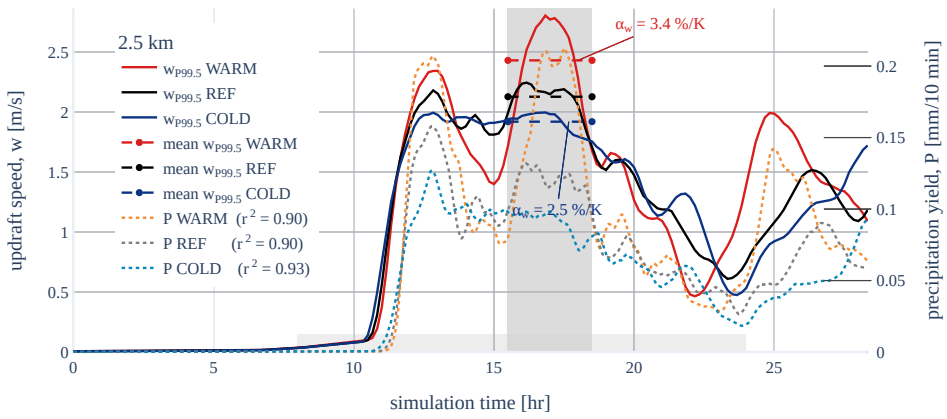
Figure A.3: Strong updrafts selected with the 99.5th percentile of vertical speeds in a cross section at 2.5 km.
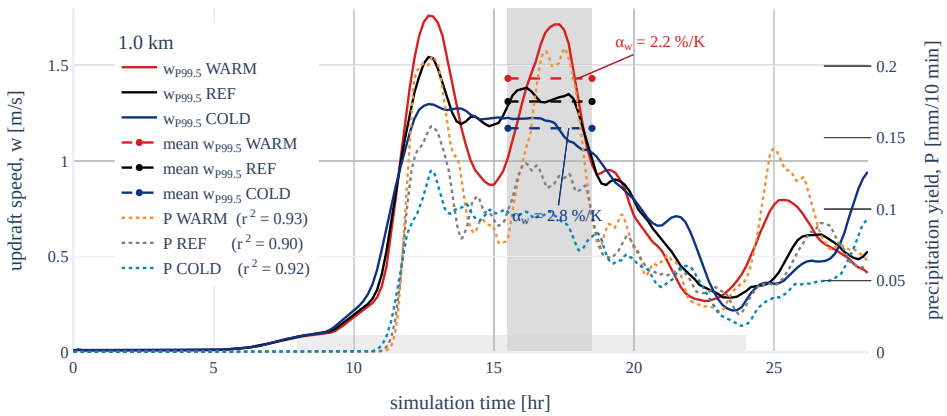
Figure A.4: Strong updrafts selected with the 99.5th percentile of vertical speeds in a cross section at 1 km.

A.2. Profiles of vertical motion scaling

In Section 5.1.2 a result is presented for the vertical profiles of strong speed scaling. Only one profile is shown there. Here, a variety of profiles for updrafts is displayed in Figure A.5. The same is done for subsiding motions in Figure A.5. The Figures show that the result in Section 5.1.2 is representative.
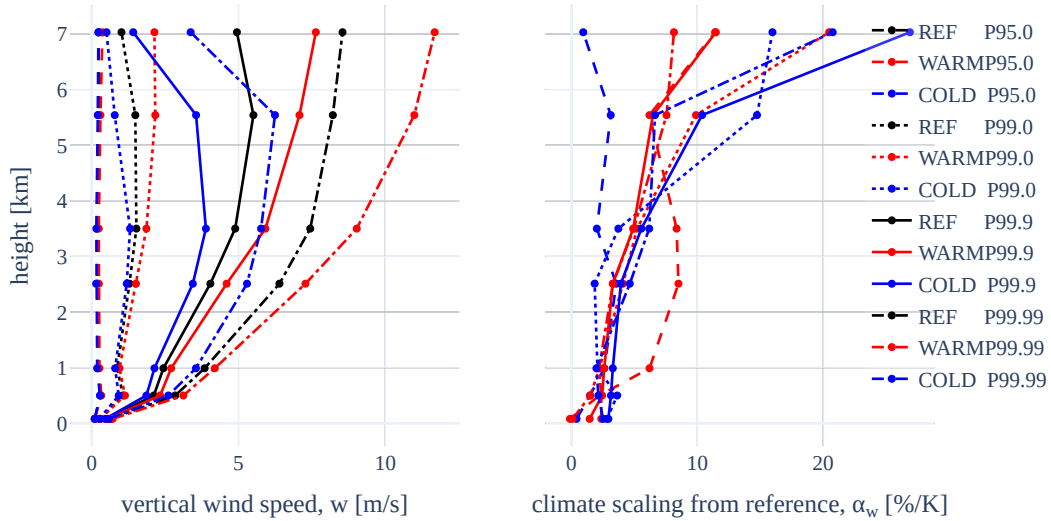
Figure A.5: Scaling of the updrafts in a height profile. In the left panel, are the profiles of the vertical wind speeds at the 95th, 99th, 99.9th and 99.99th percentiles. The sample is of all spatial points at 18 timesteps in organized phase. In the right panel are these same datapoints scaled with respect to the REF simulation.
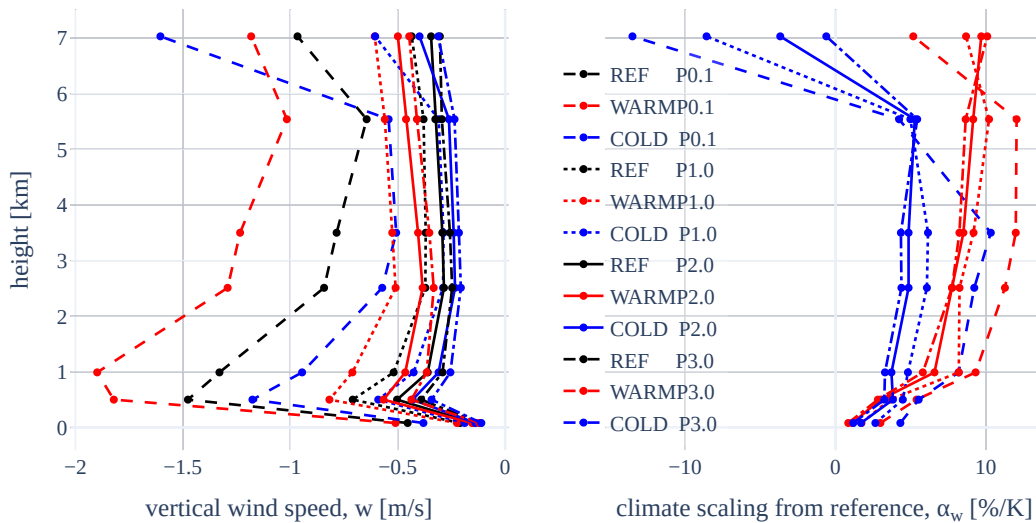
Figure A.6: Scaling of the subsiding motions in a height profile. In the left panel, are the profiles of the vertical wind speeds at the 0.1th, 1st, 2nd and 3rd percentiles. The sample is of all spatial points at 18 timesteps in organized phase. In the right panel are these same datapoints scaled with respect to the REF simulation.

B

Classifying the cross-sections

The cross-sections available are classified based on the sampled slab averaged cloud fraction. This is computed as the number of grid cells where condensed cloud water is present, $q_c > 0$, divided by the total number of grid cells. Some quantitative insight in what the available layers represent is given by looking at the contourplot of the slab mean cloud fraction in Figure B.1. The range of cloud fraction values plotted is cut to $c_{fraction} > 0.1\%$ to prevent the contouring function in matplotlib from drawing the clouded area down to the surface.
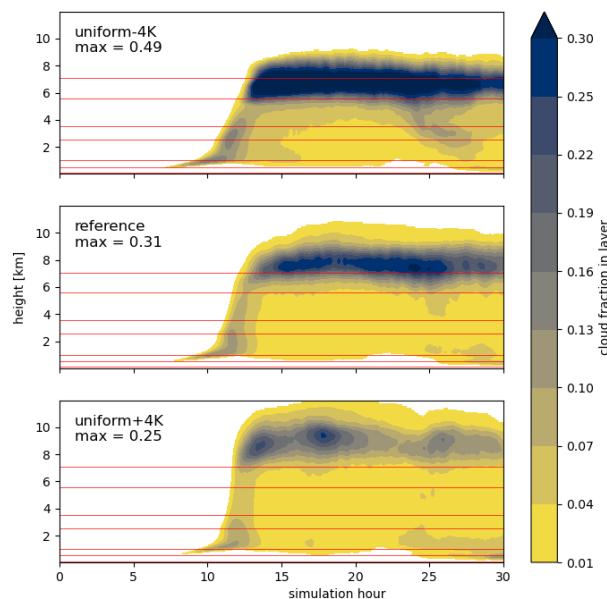
Figure B.1: Cloud fractions occurring in each of the lower 170 layers. The layers of which cross sections are available are shown as red horizontal lines. Cloud is defined here as condensed water $q_c > 0$

For the hours of interest, the lower layers can be classified as near-surface (0.1 km), sub-cloud (0.5 km) and cloud base (1 km) for all three scenario's around the time of interest (simulation hours 15:30-18:30). The cross-section layers above 1 km height can all be classified as cloud layers. During the simulations, the cloud fraction in the higher layers increases, although this is less pronounced in the warmer simulation for the threshold shown here.

61

C

Equation for the precipitation in a convective event

In an extreme event on short timescales (e.g. hourly), the precipitation is of convective nature. For such an event, it may be assumed that moisture is transported vertically whilst all moisture in excess of the saturation specific humidity is condensing in the cloud. This happens from cloud base to cloud top according the lapse rate of condensation, $\frac{\partial q_{sat}}{\partial z}$ and the mass of air being displaced with density ρ and vertical velocity w. Not all moisture transported into the cloud ultimately reaches the surface as precipitation, this is captured with the precipitation efficiency, ε.

in Section 2.1.6, the simplified Equation 2.5 is formulated similar to a volume of literature (e.g. Abbott et al., 2020; Loriaux et al., 2017; Muller & Takayabu, 2020). Here it is derived it in accordance with Muller et al. (2011). As a start, the Lagrangian derivative is defined in Equation C.1.

$$\frac{D}{Dt} = \frac{\partial}{\partial t} + \frac{\partial u}{\partial x} + \frac{\partial v}{\partial y} + \frac{\partial w}{\partial z} \tag{C.1}$$

Furthermore, dry static energy s is defined in Equation C.2.

$$s = C_p T + gz \tag{C.2}$$

A budget may be written for the vertically integrated dry static energy for the relevant part of the atmosphere, from earths surface to the tropopause (O'Gorman & Schneider, 2009) as in Equation C.3.

$$\left[\frac{Ds}{Dt}\right] \approx L_s \left[\frac{D(r_s + r_g + r_i)}{Dt}\right] + L_v \left[\frac{D(r_r + r_l)}{Dt}\right] + L_v P \tag{C.3}$$

Where the mass-weighted vertical integral from Earth's surface to the troposphere is given by:

$$[...] = \int_{surf}^{trop} (...)\bar{\rho} dz \tag{C.4}$$

In the above equations, the mixing ratios, r are given for the fractions of liquid precipitation (rain) r_r, cloud liquid water r_l, snow r_s, graupel r_g and ice r_i. L_s and L_v are latent heats of sublimation and evaporation respectively. P is precipitation, which is assumed to be in liquid phase only when reaching

the surface. The liquid surface precipitation only simplifies the contribution of precipitation to $L_v P$. The mean density profile is $\overline{\rho}(z)$. The wind speeds u, v, w are in the Cartesian directions x, y, z respectively.

Another number of approximations, listed below can be used to formulate Equation C.5. Muller et al. (2011) use these for strong precipitation in the tropics, but here they are used for mid-latitudes nonetheless.

1. Neglect water contributions to the heat capacity and the temperature dependencies of L_s and L_v.
2. Neglect the difference between L_s and L_v.
3. Subgrid-scale fluxes as well as radiative cooling are assumed negligible when strong precipitation occurs. So the energy transport is done by advection, precipitation and phase change of advected moisture.
4. The Lagrangian derivative of dry static energy is dominated by the vertical advection term $Ds/Dt = w\frac{\partial s}{\partial z}$. Muller et al. (2011) states errors of 0.5% for hourly timescales and less than 2% for daily time scales at the 99.99th precipitation percentile.
5. The dry static energy is approximated by its horizontal and time mean profile $s(z)$
6. The hydrostatic approximation is used.
7. The mean atmospheric lapse rate is approximated by the moist adiabatic lapse rate.
8. The mixing ratios are assumed equal to specific humidities. $q = r$

$$\frac{Ds}{Dt} = w\frac{\partial s}{\partial z} = C_p dT + g dz \cong -L_v \frac{\partial q_{sat}}{\partial z} \tag{C.5}$$

By now entering Equation C.5 into Equation C.3, an approximation for precipitation in an extreme event P_e can be found in Equation C.7. The fractions of snow (s), graupel (g), ice (i), rain (r) and cloud liquid water (l) could be summarized with the cloud condensed specific humidity, defined in Equation C.6.

$$q_c = q_s + q_g + q_i + q_r + q_l \tag{C.6}$$

$$P_e \cong -[w\frac{\partial q_{sat}}{\partial z}] - [\frac{D(q_s + q_g + q_i + q_r + q_l)}{Dt}] \tag{C.7}$$

By defining the precipitation efficiency ϵ, the precipitation rate for an extreme event can be written as Equation 2.5. The integral in C.7 can be written out again and it can be combined with Equation C.6. This leads to Equation 2.5, which is often found in literature. Here it is repeated again for completeness in Equation C.8

$$P_e = \varepsilon \int_{surf}^{trop} \rho w(-\frac{\partial q_{sat}}{\partial z}) dz \tag{C.8}$$

List of Tables

List of Figures